CELLULAR NEUROSCIENCE

Lysosomal dysfunction in Down syndrome and Alzheimer mouse models is caused by v-ATPase inhibition by Tyr^{682}-phosphorylated APP βCTF

Eunju Im[1,2], Ying Jiang[1,2], Philip H. Stavrides[1], Sandipkumar Darji[1], Hediye Erdjument-Bromage[3,4], Thomas A. Neubert[3,4], Jun Yong Choi[5,6], Jerzy Wegiel[7], Ju-Hyun Lee[1,2], Ralph A. Nixon[1,2,3,8]*

Lysosome dysfunction arises early and propels Alzheimer's disease (AD). Herein, we show that amyloid precursor protein (APP), linked to early-onset AD in Down syndrome (DS), acts directly via its β-C-terminal fragment (βCTF) to disrupt lysosomal vacuolar (H^+)–adenosine triphosphatase (v-ATPase) and acidification. In human DS fibroblasts, the phosphorylated ^{682}YENPTY internalization motif of APP-βCTF binds selectively within a pocket of the v-ATPase V0a1 subunit cytoplasmic domain and competitively inhibits association of the V1 subcomplex of v-ATPase, thereby reducing its activity. Lowering APP-βCTF Tyr^{682} phosphorylation restores v-ATPase and lysosome function in DS fibroblasts and in vivo in brains of DS model mice. Notably, lowering APP-βCTF Tyr^{682} phosphorylation below normal constitutive levels boosts v-ATPase assembly and activity, suggesting that v-ATPase may also be modulated tonically by phospho-APP-βCTF. Elevated APP-βCTF Tyr^{682} phosphorylation in two mouse AD models similarly disrupts v-ATPase function. These findings offer previously unknown insight into the pathogenic mechanism underlying faulty lysosomes in all forms of AD.

INTRODUCTION

The ultrastructural neuropathology of Alzheimer's disease (AD) is dominated by robust and selective buildup of autophagic vacuoles within neurons, reflecting the defective transport and clearance of autophagic waste from neurons (*1*, *2*). Abnormalities at all levels of the endosomal-lysosomal-autophagy network are an invariant early and progressive feature of AD neuropathology and pathophysiology (*1*). Accumulation of amyloid precursor protein (APP)–β-C-terminal fragment (βCTF) in lysosomes is also believed to corrupt their functioning in mouse models of AD and Down syndrome (DS, also referred to as Trisomy 21) and promote AD-related pathology (*3*–*5*).

The close association between lysosomal dysfunction and neurodegeneration is underscored by mutations of at least 30 genes operating within the endosomal-lysosomal system that cause inheritable neurodegenerative diseases across the aging spectrum (*2*, *6*). In AD, disrupted lysosome function contributes to neuritic dystrophy, reduced clearance of β amyloid and tau, synaptic plasticity deficits, and neurodegeneration (*7*–*10*). These deficits in mouse models are substantially remediated by restoring lysosomal functionality (*11*–*13*). Despite the growing evidence implicating lysosomes in pathogenesis in neurodegenerative diseases, the mechanisms underlying lysosomal system dysregulation remain unclarified.

Lumenal acidification of lysosomes to a pH of 4.5 to 5.0 is essential for their function (*14*), including optimal activation of varied hydrolytic enzymes and regulation of ion channels involved in lysosomal trafficking and cell signaling (*15*, *16*). Lysosomal acidification is maintained primarily by a vacuolar (H^+)–adenosine triphosphatase (v-ATPase), a multimeric enzyme complex that pumps protons from the cytosol into the lysosomal lumen (*14*). Fourteen protein subunits form the complete v-ATPase complex composed of two sectors: an integral membrane-associated V0 sector and a cytosolic V1 sector capable of regulated dissociation from the V0 sector. The V1 sector, comprising subunits A to H, is responsible for adenosine triphosphate (ATP) hydrolysis. The V0 sector, composed of subunits a, d, e, c, and c″, forms the channel that conducts proton transport (*17*, *18*).

v-ATPase activity is subject to various forms of regulation that modulate subunit expression, assembly, trafficking, and signaling (*18*). Among the most important is regulation of the V1 sector association with the membrane-bound V0 sector (*19*, *20*). Cryogenic electron microscopy analysis showed that ATP hydrolysis in the soluble catalytic region (V1 sector) of v-ATPase is coupled to proton translocation through the membrane-bound region (V0 sector) by rotation of a central rotor subcomplex, with peripheral stalks preventing the entire membrane-bound region from turning with the rotor (*21*). Thus, to form a functional channel of v-ATPase, assembly of V0 sector and V1 sector is a necessary event. Physiological changes in v-ATPase activity modulate nutrient sensing that controls mammalian target of rapamycin (mTOR) activity, autophagy induction, and lysosomal biogenesis (*15*, *22*, *23*). Mutations of v-ATPase subunits cause nearly a dozen familial degenerative diseases, most having a substantial central nervous system phenotype (*24*). v-ATPase components are most highly

[1]Center for Dementia Research, Nathan S. Kline Institute, Orangeburg, NY 10962, USA. [2]Department of Psychiatry, New York University Grossman School of Medicine, New York, NY 10016, USA. [3]Department of Cell Biology, New York University Grossman School of Medicine, New York, NY 10016, USA. [4]Kimmel Center for Biology and Medicine at the Skirball Institute, New York University Grossman School of Medicine, New York, NY, 10016, USA. [5]Department of Chemistry and Biochemistry, Queens College, Queens, NY 11367, USA. [6]Ph.D. Programs in Chemistry and Biochemistry, The Graduate Center of the City University of New York, New York, NY 10016, USA. [7]Department of Developmental Neurobiology, New York State Institute for Basic Research in Developmental Disabilities, Staten Island, NY 10314, USA. [8]NYU Neuroscience Institute, New York University Grossman School of Medicine, New York, NY 10016, USA.
*Corresponding author. Email: ralph.nixon@nki.rfmh.org

expressed in neurons, and activity is regulated by various signaling cascades that likely contribute to the way different risk factors compromise lysosomes in AD (*24*). Notably, we found that familial early-onset AD due to *PSEN1* mutation disrupts maturation and lysosomal delivery of v-ATPase V0a1 subunit, thus impairing v-ATPase assembly and proton pumping and leading to diverse features of AD pathophysiology (*25*).

In this study, we show that APP, like *PSEN1* in AD, disrupts v-ATPase complex assembly and lysosomal acidification by a distinctive mechanism that also directly involves the V0a1 subunit. We demonstrate that phospho-Tyr^{682}-APP-βCTF (pY^{682}APP-βCTF) generated by β-secretase (BACE1) cleavage from constitutively phosphorylated APP selectively and directly interacts with the cytoplasmic domain of the V0a1 subunit. This interaction impedes association of V1 subunits thereby inhibiting v-ATPase activity and acidification of lysosomes. Levels of pY^{682}APP-βCTF can rise by multiple mechanisms, including elevated APP expression, increased BACE1 activity, underactive protein phosphatases, or an overactive Tyr kinase. Regardless of which combination of the foregoing mechanisms operates in DS or AD, we show that lowering APP Tyr^{682} phosphorylation pharmacologically can prevent the disruptive effects of APP-βCTF on lysosome function in vivo. Our results and growing knowledge of AD pathobiology support our view that v-ATPase disruption is a primary triggering mechanism in AD and that v-ATPase dysregulation is a previously unidentified therapeutic target. Last, our initial evidence that lowering APP levels or APP-βCTF itself below baseline endogenous levels accentuates v-ATPase assembly and activity, raises the possibility of tonic modulation of lysosomal function by APP in physiological states as well as in disease. Our findings reported here and other emerging data (*8*, *26*) point toward a unifying pathogenic mechanism underlying primary lysosomal dysfunction in AD.

RESULTS

Lysosomal v-ATPase dysfunction in DS fibroblasts is caused by impaired complex assembly

We confirmed that lysosomal acidification is impaired in DS fibroblasts (*5*) by measuring lysosomal pH using LysoSensor Yellow/Blue dextran, a ratiometric dye targeted to lysosomes (*27*). Lysosomal pH was significantly increased in DS fibroblasts compared to control (2N) (Fig. 1A). Consequently, the activity of the lysosomal hydrolase, cathepsin D (CTSD), is impaired in DS fibroblasts (*5*). Because lysosome acidity is generated mainly by v-ATPase (*14*), we measured lysosomal v-ATPase activity by using a superparamagnetic chromatography isolation procedure (*28*) to isolate highly enriched lysosomal preparations from DS and 2N cells, the purity of which is reflected by the high level of lysosomal associated membrane protein 1 (LAMP1) enrichment (fig. S1). We then measured the rate of ATP hydrolysis in purified lysosomes monitored by release of inorganic phosphate, which revealed ~40% lower rates in lysosomes isolated from DS fibroblasts relative to 2N (Fig. 1B). To confirm the predicted impact of this lowered ATP hydrolysis, we measured the rates of proton translocation into the lysosomal lumen using the quenching of 9-amino-6-chloro-2-methoxyacridine (ACMA), which uncovered an ~80% lower rate in purified lysosomes from DS fibroblasts than from 2N lysosomes (Fig. 1, C and D).

The v-ATPase complex is only active when the membrane-bound V0 sector and the cytosolic V1 sector are assembled on the lysosomal membrane (*20*). We examined the assembly of the v-ATPase complex using native polyacrylamide gel electrophoresis (PAGE) followed by mass spectrometry (MS) analysis. On native PAGE gels, the fully assembled v-ATPase (about 880 kDa) was present at significantly reduced in DS fibroblasts as compared to 2N cells (Fig. 1E; "Full"). Furthermore, DS cells contained elevated levels of incompletely assembled subcomplexes exhibiting increasing mobility on the native gel, which correlated with detection of fewer V1 subunits associated with V0 in the membrane fraction (Fig. 1E; "Sub"). The relative ratio of fully assembled v-ATPase divided by total v-ATPase (fully assembled v-ATPase plus subcomplexes of v-ATPase bands) revealed ~35% lower ratios in DS fibroblasts as compared to 2N (Fig. 1F). This indicates that decreased lysosomal v-ATPase activity was due to reduced levels of the fully assembled functional v-ATPase complex formation in DS fibroblasts. The bands of v-ATPase were detected with a V1B2 subunit antibody and shown by MS analysis to contain all V1 subunits (fig. S2). To further investigate the possible disruption of v-ATPase assembly in DS cells, we examined v-ATPase complex assembly on cell membranes separated from the cytosol, each subjected to immunoblot analysis. Because affinities of the specific antibodies differ for each subunit, the relative abundance of subunits cannot be compared by band intensity; however, the membrane (Memb): cytosol (Cyto) ratio for each subunit is a reliable index of the changes in degree of association of a given V1 subunit with the V0 sector. The Memb:Cyto ratios for all of the V1 subunits were significantly lowered in DS fibroblasts (Fig. 1, G and H).

Because APP-βCTF is implicated in lysosomal dysfunction (*3*, *5*) and accumulate in lysosome-related compartments in AD and DS models, we next investigated v-ATPase assembly and function using lysosome-enriched (Lyso) fractions, which indeed demonstrated a disproportionate v-ATPase deficit relative to the total cellular v-ATPase pool. All V1 subunits in purified lysosomes from DS fibroblasts were present at markedly decreased levels compared to those in the Lyso fraction from 2N cells (Fig. 1, I and J). These findings on isolated lysosomes were confirmed by further results from double-immunofluorescence labeling analyses that revealed strong colocalization of V1D subunit with cathepsin B (CTSB)–positive compartments in 2N cells (Fig. 1K). Quantitative analyses of colocalization with lysosomes showed a significantly decreased lysosomal colocalized V1D level in DS fibroblasts (Fig. 1L). We confirmed lysosomal pH, v-ATPase activity and assembly, and localization of V1 subunits in another line of DS fibroblasts (5-month-old) compared to age matched control (2N) fibroblasts (fig. S3). Together, the foregoing data indicated that dysfunction of v-ATPase activity is related to a markedly lowered association of the V1 sector with the V0 sector on lysosomal membranes in DS fibroblasts.

APP-βCTF modulates v-ATPase activity and is inhibitory at elevated levels in DS

In light of previous studies linking APP-βCTF to lysosomal dysfunction in AD, DS, and AD models (*3*, *5*, *8*), we investigated whether the mechanism of the underlying lysosomal v-ATPase deficits in DS fibroblasts was due to elevated generation of APP-βCTF from the extra *APP* gene copy (3N). We knocked down APP expression to levels below those in 2N control cells using small interfering RNA (siRNA) constructs specifically against human *APP* (siAPP)

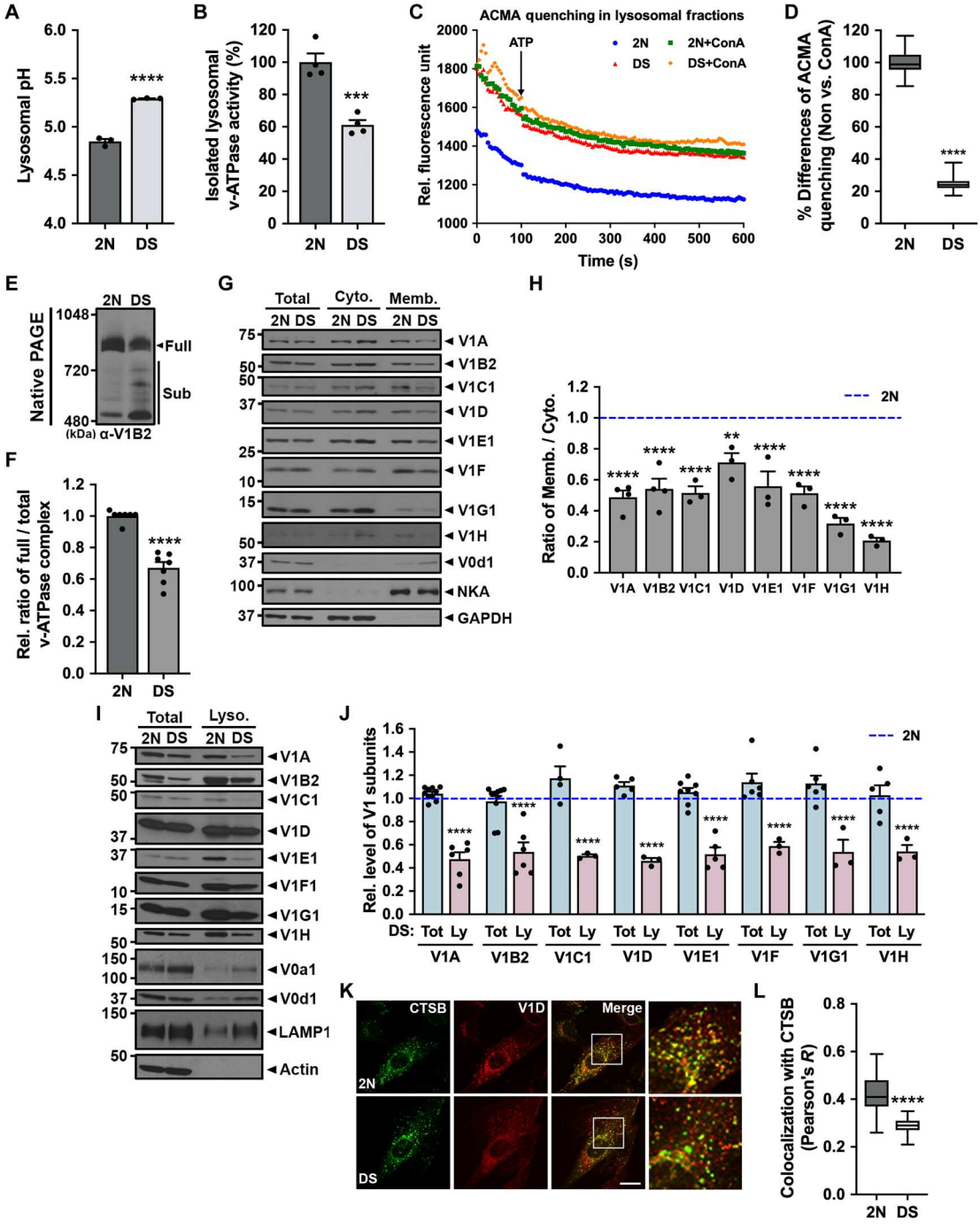

Fig. 1. Assembly of the lysosomal v-ATPase complex is impaired in 2year DS fibroblasts. (**A**) Lysosomal pH measured ratiometrically using LysoSensor Yellow/Blue (Y/B) dextran (n = 3, three independent, triplicate). (**B** to **D**) Lysosomal v-ATPase activity measured colorimetrically as ATP hydrolysis (B) (n = 4, four independent, duplicate) and fluorometrically (ACMA method) as H^+ transport (C and D) (n = 3, three independent) using Lyso fractions. (**E**) Membrane fractions were resolved using native PAGE and immunoblotted with anti-V1B2 antibody. (**F**) The graph represents relative ratio of full complex divided by total (full plus sub complexes) complexes of v-ATPase (n = 7, seven independent). (**G**) Immunoblots of v-ATPase subunits distribution in cytosol (Cyto.) and membrane (Memb.) fractions of 2N and DS fibroblasts. Na, K-ATPase 1 (NKA) served as a Memb. marker, and glyceraldehyde-3-phosphate dehydrogenase (GAPDH) served as a Cyto. marker. (**H**) The graphs represent the ratio of Memb. versus Cyto. band of each v-ATPase subunits ($n \geq 3$, at least three independent). (**I**) Immunoblot of v-ATPase subunit distributions in total lysates (Total) and lysosome-enriched (Lyso.) fractions. LAMP1 served as a marker for lysosomes, and actin served as a loading control for total lysates. (**J**) The graphs show relative band intensity for each v-ATPase subunit ($n \geq 3$, at least three independent). (**K** and **L**) Double-immunofluorescence labeling shows colocalization of v-ATPase (V1D) and CTSB (K). Scale bar, 10 μm. Quantification analysis of v-ATPase V1D and lysosomal marker, CTSB, shows colocalization as calculated by Pearson's correlation coefficient ($n \geq 131$ cells, three independent) (L). Quantitative data are presented as mean values with ±SEM, two-tailed unpaired t test (A, B, D, F, and L), ordinary one-way analysis of variance (ANOVA) with Šidák's multiple comparisons test (H), ordinary two-way ANOVA with Šidák's multiple comparisons test (J). Each dot represents average value of technical replicates from each independent experiment.

and compared these cells to those exposed to scrambled RNA sequences (siNC). Knockdown of APP, confirmed by Western blot (WB) 72 hours after siRNA transfection, significantly rescued lysosomal pH (Fig. 2A) and v-ATPase activity (Fig. 2B) in DS fibroblasts. Moreover, the same treatment restored assembly of the v-ATPase complex (Fig. 2, C and D) with a full complement of V1 subunits (Fig. 2, E and F) in DS fibroblasts. These data therefore indicate that, even in the presence of the entire extra copy of Chr.21 in DS cells, v-ATPase dysfunction is dependent mainly on the extra copy of *APP*. Unexpectedly, knockdown of APP in 2N fibroblasts further lowered lysosomal pH by 0.11 pH units, which was associated with significantly higher v-ATPase activity (16%). Moreover, levels of V1 subunits associated with lysosomes were significantly higher while corresponding levels in the cytosol were lowered, consistent with an increased assembly of v-ATPase complex on lysosomes in 2N control fibroblasts with APP levels below normal baseline. These findings in 2N fibroblasts and additional data discussed later suggest that v-ATPase may be tonically modulated by APP.

APP-βCTF levels are elevated in AD and DS brain (*29*, *30*) and rise substantially in lysosomes (*3*, *5*). We observed that these increases in DS fibroblasts (*5*) are accompanied by lysosomal pH elevation (Fig. 3A). We addressed the specificity of APP-βCTF as a mediator of this effect by first measuring v-ATPase activity in lysosomes from cells treated with vehicle or γ-secretase inhibitor L685,458 (γ-Sec INH), which elevates APP-βCTF levels (fig. S4A)

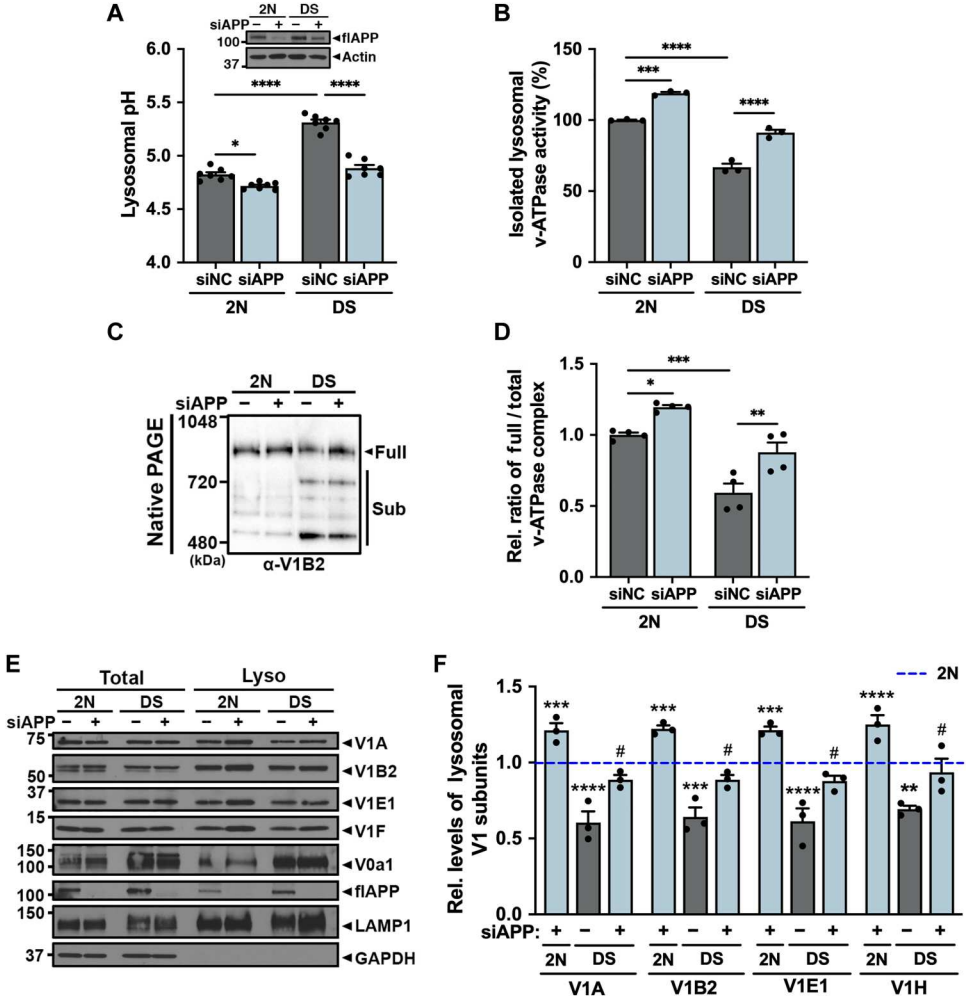

Fig. 2. Impairment of lysosomal v-ATPase in 2-year DS fibroblasts is dependent on APP expression. (**A**) Lysosomal pH of 2N and DS fibroblasts transfected with siRNA for either negative control (siNC) or APP (siAPP) for 72 hours determined by LysoSensor Y/B dextran ($n = 7$, seven independent, quadruplicate). The immunoblot represents APP levels in 2N and DS fibroblasts after transfection with 40 nM siNC or siAPP. (**B**) ATP hydrolysis activity of v-ATPase measured using lysosomal fractions from siRNA transfected 2N and DS fibroblasts ($n = 3$, three independent, duplicate). (**C**) Membrane fractions of siRNA transfected 2N and DS fibroblasts were resolved using native PAGE and immunoblotted with anti-V1B2 antibody. (**D**) The graph represents relative ratio of full complex divided by total (full plus sub complexes) complexes of v-ATPase ($n = 4$, four independent). (**E**) Immunoblots of v-ATPase subunit distributions in total and Lyso. fractions of siRNA transfected 2N and DS fibroblasts. LAMP1 served as a Lyso marker and GAPDH served as a loading control for total lysates. (**F**) The graphs show band intensity of each v-ATPase subunit from Lyso fraction ($n = 3$, three independent). Quantitative data are presented as mean values with ±SEM, ordinary one-way ANOVA with Šidák's multiple comparisons test (A, B, and D) and ordinary two-way ANOVA with Šidák's multiple comparisons test (F). Statistical significance between groups is shown by symbols: *2N + siNC versus others, #DS + siNC versus DS + siAPP. Each dot represents average value of technical replicates from each independent experiment.

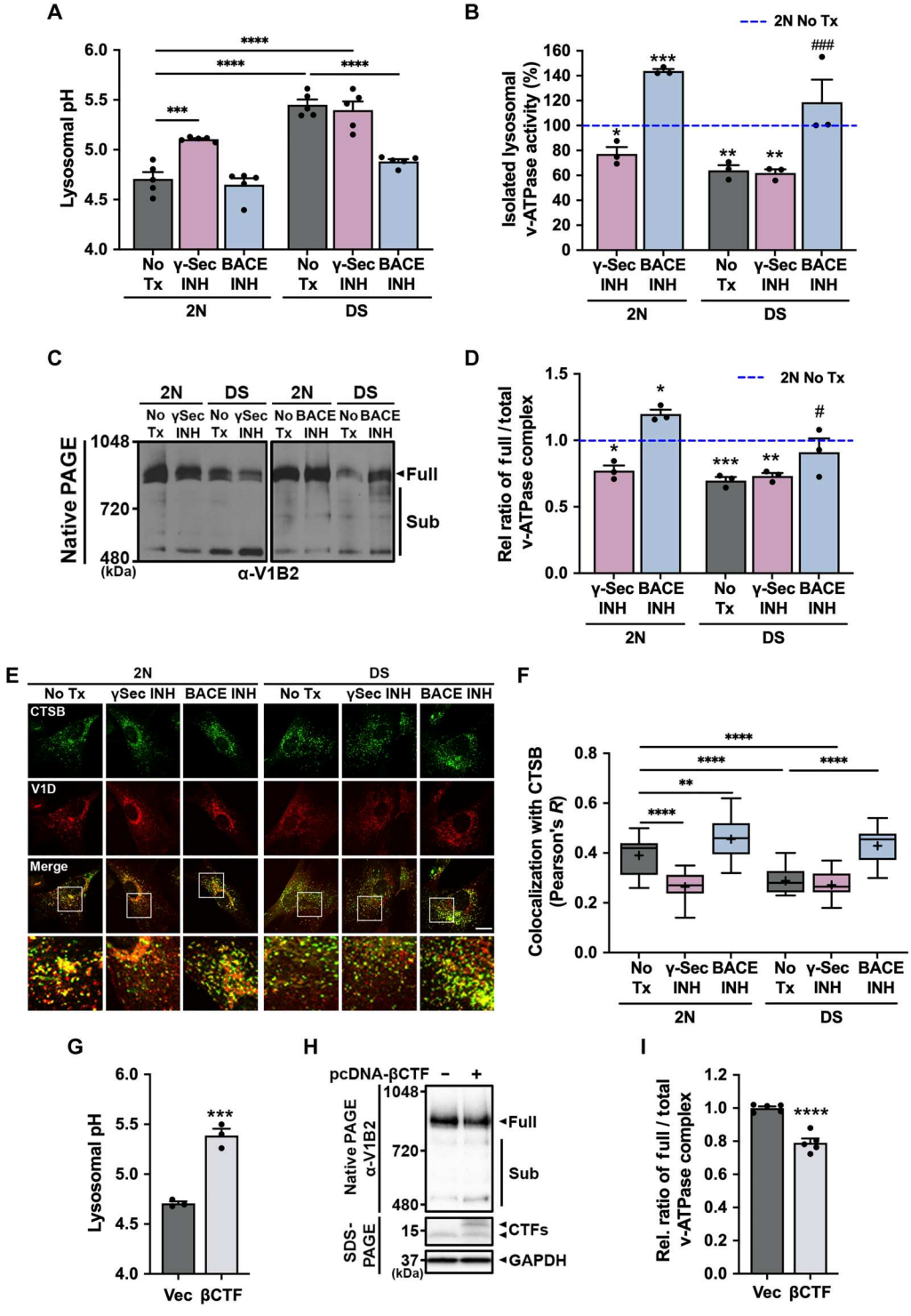

Fig. 3. Lysosomal v-ATPase activity is specifically affected by APP-βCTF among metabolites of APP. (**A**) Lysosomal pH of 2-year 2N and DS fibroblasts treated with either dimethyl sulfoxide (DMSO) (No Tx), γ-secretase inhibitor, L685,458 (γ-Sec INH; 10 μM), or BACE1 inhibitor (BACE INH; 10 μM) for 24 hours determined by LysoSensor Y/B dextran (n = 5, five independent, triplicate). (**B**) ATP hydrolysis activity of v-ATPase measured using lysosome fractions from 2-year 2N and DS fibroblasts after treatment indicated inhibitors (n = 3, three independent, duplicate). (**C**) Membrane fractions from 2-year 2N and DS fibroblasts treated with indicated inhibitors were resolved using the native PAGE and immunoblotted with anti-V1B2 antibody. (**D**) The graph represents relative ratio of full complex divided by total (full plus sub complexes) complexes of v-ATPase (n = 3, three independent). (**E** and **F**) Double-immunofluorescence labeling shows colocalization of V1D and CTSB in 2N and DS fibroblasts treated with indicated inhibitors (E). Scale bar, 10 μm. Quantification analysis shows colocalization as calculated by Pearson's correlation coefficient ($n \geq$ 123 cells, three independent) (F). (**G**) Lysosomal pH of 2-year 2N fibroblasts transfected with either empty vector (Vec) or pcDNA-APP-βCTF (βCTF) for 48 hours determined by LysoSensor Y/B dextran (n = 3, three independent, triplicate). (**H**) Membrane fractions from 2-year 2N transfected with either empty vector (–) or pcDNA-APP-βCTF (+) for 48 hours were resolved using the native PAGE and immunoblotted with anti-V1B2 antibody. (**I**) The graph represents relative ratio of full complex divided by total complexes of v-ATPase (n = 5, five independent). Quantitative data are presented as mean values with ±SEM, ordinary one-way ANOVA with Šidák's multiple comparisons test (A, B, D, and F) and two-tailed unpaired t test (G and I). Statistically significance between groups is shown by symbols: *2N No Tx versus others, #DS No Tx versus DS + inhibitor. Each dot represents average value of technical replicates from each independent experiment.

by inhibiting its γ-cleavage to form Aβ peptide (*31*). In 2N cells, γ-Sec INH elevated APP-βCTF levels and strongly inhibited v-ATPase activity (Fig. 3B). In DS fibroblasts where APP-βCTF is already elevated and v-ATPase activity is disrupted, an additional impact of γ-Sec INH was not detected (Fig. 3B). We observed this same pattern of DS phenotype induction in 2N cells when assembly of lysosomal v-ATPase was assessed by native gel analysis (Fig. 3, C and D) or CTSB and V1D colocalization was assayed by double-label immuno-flouro cytochemistry (IFC) (Fig. 3, E and F).

In contrast to effects of γ-Sec INH, lowering APP-βCTF generation from APP by using BACE1 inhibitor IV (BACE INH) (fig. S4B) almost fully recovered lysosomal pH (Fig. 3A) and function of v-ATPase in DS fibroblasts (Fig. 3, B to F). Further supporting the concept that APP may tonically modulate v-ATPase activity,

v-ATPase function in 2N fibroblasts was enhanced by BACE INH, similar to observations in the siAPP studies (Fig. 2B), ATPase activity rose significantly (50%) above baseline activity in BACE INH–treated 2N cells (Fig. 3B) associated with significantly enhanced v-ATPase complex assembly (Fig. 3, C and D) and V1D colocalization with CTSB-positive lysosomes (Fig. 3, E and F). Furthermore, lysosomal pH trended nonsignificantly toward a lower than baseline level (Fig. 3A). In addition, the effects of APP-βCTF on lysosomal pH and v-ATPase assembly were directly demonstrated by overexpressing APP-βCTF in 2N fibroblasts. Our results showed that transient transfection of APP-βCTF significantly elevated lysosomal pH (Fig. 3G), decreased v-ATPase assembly by 21% (Fig. 3 H and I), and reduced CTSD-specific activity (*5*) in 2N fibroblasts. These findings provide direct evidence for the pathological action of APP-βCTF on lysosomes.

To rule out an effect of APP-αCTF on v-ATPase function, we blocked its generation in cells using the selective α-secretase inhibitor, tumor necrosis factor α protease inhibitor-1 (TAPI-1) (*32*), which reduced APP-αCTF levels by 30 to 50% (fig. S4C). No discernible changes of lysosomal pH (fig. S4D), v-ATPase activity (fig. S4E) or v-ATPase assembly (fig. S4, F and G) were seen in 2N and DS fibroblasts after exposure to TAPI-1. Together, the foregoing data indicated that v-ATPase is specifically regulated by APP-βCTF and suggested that the baseline level of v-ATPase function in 2N fibroblasts reflects a tonic balance that can be potentially modulated by APP-βCTF levels.

APP-βCTF binds selectively to v-ATPase via its YENPTY domain and depends on Tyr^{682} APP phosphorylation

A previous synaptic interactome analysis of the APP intracellular domain (AICD) revealed APP-interacting proteins associated with presynaptic vesicle synaptic termini including several v-ATPase subunits, such as V0a1, V0d1, V1A, V1B2, V1C, V1D, and V1E (*33*). On the basis of this clue, we investigated whether APP interacts with v-ATPase subunits by performing co-immunoprecipitation (IP) analyses in 2N and DS fibroblasts. In control 2N cell lysates, V0a1, V0d1, V1A, V1B2, V1D, and V1E1 were pulled down in IP using C1/6.1 antibody against the extreme C-terminal sequence of APP (amino acid residues 676 to 695 of human APP 695 isoform) but not in IP using a nonspecific control antibody (immunoglobulin G) (Fig. 4, A and B, left). The binding of APP with V1 subunits (V1A, V1B2, V1D, and V1E1) was decreased in DS cell lysates (Fig. 4B, left), while APP strongly interacted with V0 subunits (V0a1 and V0d1) (Fig. 4A, left). We calculated the extent of binding reflected by the quantitative value of IP-ed subunits divided by the protein level (lysate) and IP-ed APP (fig. S5, A and B). This result suggested that the binding with APP and v-ATPase subunits changed in DS compared to control 2N fibroblasts, although the protein level of V0a1 was changed (fig. S5, C and D).

To establish a lysosomal localization of the interaction between APP and v-ATPase subunits, we performed co-IP assays using a Lyso fraction. APP showed elevated interaction with V0a1/V0d1 in the Lyso fraction of DS fibroblasts (Fig. 4C). By contrast, APP did not interact with V1 subunits (V1A, V1B2, V1D, and V1E1) in the Lyso fraction (Fig. 4C).

Because C1/6.1 IP analyses of APP interaction with V0a1 in Fig. 4A (lysates) and Fig. 4C (lysosomes) do not discriminate whether the V0 subunit interacts with full-length APP (flAPP) or APP-βCTF, we performed additional co-IP assays using V0a1 antibody. V0a1 pulled down APP-βCTF but not flAPP (Fig. 4D). In addition, we confirmed the increased interaction between APP-βCTF and V0a1 in DS fibroblasts compared with 2N cells by an in situ proximity ligation assay (PLA) (*34*) using a Duolink technology involving two primary antibodies to V0a1 and APP (C1/6.1) followed by the addition of secondary antibodies fused to oligonucleotide proximity probes (Fig. 4E, left diagram). The proximity probes ligate with connector oligonucleotides to form a circular DNA strand when two proteins are within 40 nm of each other, allowing signal amplification and subsequent binding of fluorescently labeled probes. PLA fluorescence (red dots) was detected in DS fibroblasts at considerably higher levels than in controls (Fig. 4, E and F).

The C-terminal region of APP contains the ^{682}YENPTY internalization motif with an NPXpY element, a typical internalization signal for membrane proteins (*35*). The conserved motif is important for interactions with specific cytosolic proteins, including Fe65-PTB2 and Grb2-SH2 that regulate APP metabolism and signaling (*36*, *37*). Among three Tyr residues present in the AICD, only Tyr^{682} is phosphorylated in vivo (*36*). Both APP phosphorylation and total APP-βCTF levels are increased in AD brain (*38*, *39*). A rise in total APP-βCTF will elevate cell levels of pY^{682}APP-βCTF, irrespective of whether APP phosphorylation state increases above its constitutive level. To investigate the interaction between V0a1 and the ^{682}YENPTY motif, we synthesized an unphosphorylated peptide (QNGYENPTY, Pep-1), a phosphorylated peptide (QNG^{P}YENPTY, Pep-2), and a control peptide (QNG^{P}YENVTY, Pep-3). Pep-3 is expected to reduce binding to partner proteins due to a conformation change caused by the loss of β-turn conformation at pY+3 (*36*). Cell lysates from 2N and DS fibroblasts were incubated with each peptide for 24 hours at 4°C and then IP-ed with C1/6.1 antibody. The increased APP binding with V0a1 in DS fibroblasts was decreased by only Pep-2, and this occurred in a dose-dependent manner (Fig. 5A). In addition, we directly added peptides to cells for 24 hours at 37°C, washed out the peptide-containing medium, and then added LysoSensor Yellow/Blue dextran for 24 hours at 37°C. Incubation of 2N fibroblasts with Pep-2, but not Pep-1, mimicked the effect of APP-βCTF elevation in raising the pH of lysosomes to the abnormally high pH in DS fibroblasts (Fig. 5B). Furthermore, to test direct effect of Pep-2 to v-ATPase assembly, we added peptides to 2N fibroblasts for 24 hours at 37°C, washed out the peptide-containing medium, and then examined the assembly of the v-ATPase complex using native PAGE. As expected, the v-ATPase assembly was disrupted by Pep-2 (Fig. 5, C and D). To confirm no effect of $A\beta_{1-42}$ on v-ATPase or lysosomal pH, we performed the same experiments as in Fig. 5 (A and B) by incubating cell lysates (fig. S6A) or intact cells (fig. S6B) respectively with $A\beta_{1-42}$. As expected, $A\beta_{1-42}$ peptide had no effect on binding of APP with V0 subunits (fig. S6A) or on lysosomal pH (fig. S6B). To confirm a specific interaction between phosphorylated APP and v-ATPase subunits, we carried out a series of co-IP analyses in cell lysates using anti-APP (phospho-Tyr^{682}; pY682) antibody. The binding of pY^{682}CTF with V0a1 subunit was increased in DS fibroblasts (Fig. 5E), as evidenced by the higher level of IP-ed V0a1 subunit.

On the basis of the foregoing results, we analyzed a known AICD structure complexed with Grb2-SH2 [Protein Data Bank (PDB) code: 3MXC] (*36*) to find the binding region in the V0a1 subunit. The phosphate unit of Tyr^{682} is projected toward a pocket

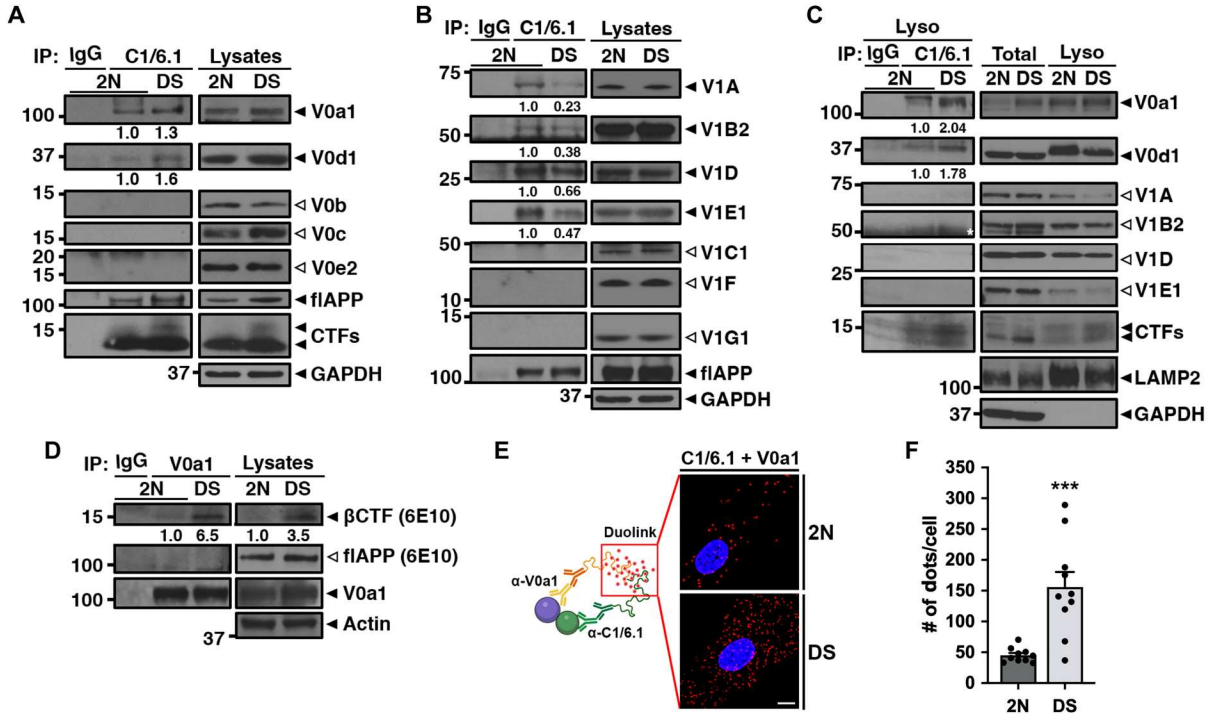

Fig. 4. The interaction between APP-βCTF v-ATPase V0 subunits increased in the lysosome-enriched fraction from 2-year DS fibroblasts. (**A** to **C**) Cell lysates (A and B) or Lyso fraction (C) of 2N and DS fibroblast were immunoprecipitated (IP-ed) with anti-APP (C1/6.1) antibody, followed by immunoblotting (IB) with antibodies of v-ATPase V0 subunits (A and C) and V1 subunits (B and C). The values at the bottom of the left IP-ed blot indicate the relative intensities of IP-ed V0a1 and V0d1 normalized by IP-ed APP. The quantification in these experiments is confirmed in two other experiments. (**D**) Cell lysates of 2N and DS fibroblast were IP-ed with anti-V0a1 antibody, followed by IB with anti-APP (6E10). Nonspecific immunoglobulin G (IgG) used as a control IP against 2N cells. The values at the bottom of the left IP blot indicate the relative intensities of IP-ed APP-βCTF normalized against IP-ed V0a1. Actin and GAPDH served as a loading control and LAMP2 served as a lysosomal marker. (**E**) Left: Schematic diagram of in situ PLA. PLA performed using V0a1 antibody and C1/6.1 for APP C terminus in 2N and DS fibroblasts. The red box represents signal of PLA (Duolink). Right: Representative fluorescent microscopy image of PLA signals demonstrating association of APP with the V0a1. Scale bar, 10 μm. (**F**) The graph show number (#) of dots per cell ($n \geq 173$ cells, three independent). Quantitative data is presented as mean values with ±SEM, two-tailed unpaired *t* test (F). Each dot represents number of dot per field of each independent experiment.

composed of R67, R86, S88, S90, S96, and K109 (fig. S7A). The phosphate group forms a hydrogen bonding interaction with S88, S90, and S96 and salt bridge interaction with R67 and R86. Three methylene units of K109 show π-hydrophobic contact with the phenyl ring of Y682 (fig. S7A). Thus, the structural features of the phospho-Y (pY) binding pocket provide for electrophilic and hydrophobic interactions and stabilize the pY in the pocket. The V0a1 subunit of mammalian brain v-ATPase (PDB code: 6VQ7), defined from a cryo–electron microscopy (cryo-EM) structure, was analyzed to locate the potential binding site of the pYENPTY motif (*40*). The cryo-EM structure includes an unsolved region from residues 667 to 712 in the V0a1 subunit (fig. S7B, green), and it has three consecutive serine residues (S151, S152, and S153) that are highly conserved among species (fig. S7C). In addition, a basic residue, R198, is located in the middle of the N and C termini of the unsolved region (fig. S7B). Thus, we speculated that this region could form a potential binding pocket for the pYENPTY motif. Moreover, two of three serine residues of the loop could be a part of the binding pocket and provide hydrogen bonding interaction to the phosphate group of the tyrosine residue. Molecular modeling, molecular dynamics (MD) simulation, and docking studies were iteratively conducted to build the pocket and estimate the binding pose of the pYENPTY motif (*41*, *42*). The model structure shows that the phosphate group of pY has hydrogen bonding interaction with S151, S153, and T250 and has a salt bridge interaction with R198 (Fig. 5, F and G). The phenyl ring of pY forms hydrophobic contacts with the methylene units of R167 and F170 in a way similar to that shown for the Grb2-SH2 and AICD complex (fig. S7A). Furthermore, MD simulation followed by molecular mechanics generalized Born surface area (MM-GBSA) calculation (*43*) shows the estimated binding affinity of the phosphorylated peptide to the pocket is more stable than its unphosphorylated counterpart ($\Delta\Delta G_{bind} = -85.6$ kcal/mol versus -67.8 kcal/mol). Together, these analyses strongly suggest that APP-βCTF interacting specifically with V0a1 modulates docking of the V1 sector to the V0 sector and that Tyr^{682} phosphorylation on the ^{682}YENPTY motif of APP plays a crucial role in this interaction.

Decreasing the levels of phospho-Y^{682} APP-βCTF rescues v-ATPase dysfunction in DS

In further investigations on the effect of Tyr^{682} phosphorylation on v-ATPase function, we found, as expected, elevated levels of pY^{682}APP-βCTF in DS fibroblasts (Fig. 6A). Given the possibility that Fyn kinase, which binds the ^{682}YENPTY motif of APP and increases APP tyrosine phosphorylation in AD neurons (*44*), represents one possible source for the elevation of pY^{682}APP-βCTF

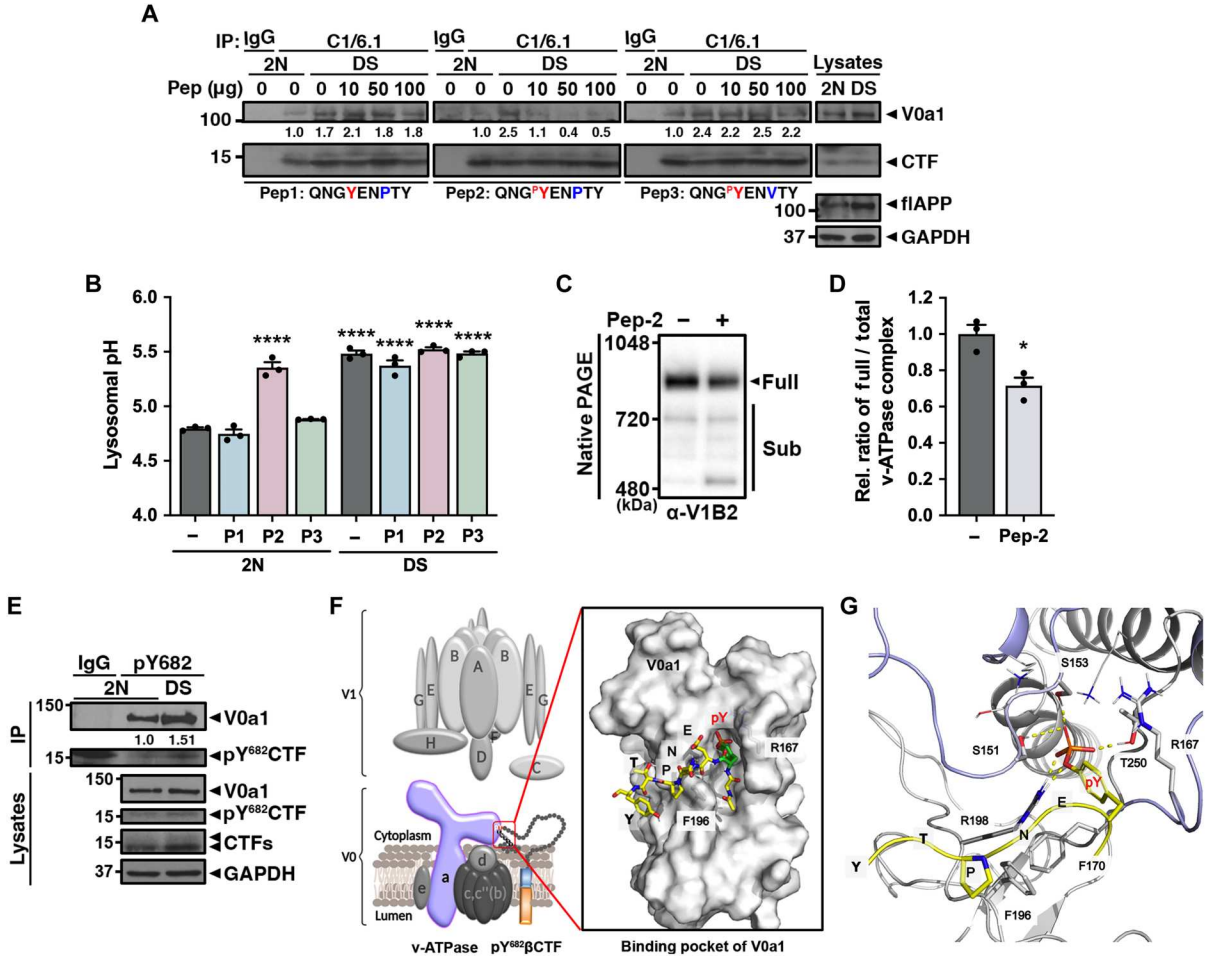

Fig. 5. pYENPTY motif of APP-βCTF interrupt the lysosomal pH via interaction with V0a1 that form a structural pocket within the complex. (**A**) Cell lysates were incubated with varying amounts of each peptide for 24 hours, then IP with anti-APP (C1/6.1) antibody, followed by IB with anti-V0a1 antibody. (**B**) Lysosomal pH measured after treated with either DMSO (–) or 5 μM peptides for 24 hours ($n = 3$, three independent, triplicate). (**C**) Membrane fractions from 2-year 2N treated with either DMSO (–) or 5 μM Pep-2 (+) for 24 hours were resolved using the native PAGE. (**D**) The graph represents relative ratio of full complex divided by total complexes of v-ATPase ($n = 3$, three independent). (**E**) Cell lysates were IP-ed with anti-pY^{682}APP antibody, followed by IB with anti-V0a1 antibody. The values at the bottom of the left IP blot indicate the relative intensities of IP-ed V0a1 normalized against IP-ed APP-CTFs (A) or pY^{682}βCTF (E). The quantification in this experiment is confirmed in two other experiments. (**F**) Schematic diagram of binding with V0a1 and pY^{682}APP-βCTF (left). The surface of the pYENPTY binding pocket of V0a1 (right) is labeled with F196 and R167 of V0a1 subunits. (**G**) The binding poses of the pYENPTY in the pocket of V0a1. Hydrogen bond and salt bridge interactions by S151, S153, R198, and T250 are labeled with yellow dash lines. The methylene units of R167 and F170 form π-hydrophobic contacts with the aromatic ring of the pY^{682}. Proline at the pY+3 position has π-hydrophobic interaction with F196. The pYENPTY is yellow and the unsolved region is light blue. Quantitative data are presented as mean values with ±SEM, ordinary one-way ANOVA with Šidák's multiple comparisons test (B), two-tailed unpaired *t* test (D). Each dot represents average value of technical replicates from each independent experiment.

levels in DS fibroblasts, we tested whether saracatinib (AZD0530), a Src family of nonreceptor tyrosine kinases inhibitor with high potency for Fyn, would lower pY^{682}APP-βCTF levels and, most importantly, rescue v-ATPase deficits. Testing with various concentrations of AZD0530 revealed a partial reduction of phospho-Y^{420}-Fyn (pFyn) at 2 μM AZD0530 (fig. S8A) indicating inhibited activity. Next, measurements of lysosomal pH and v-ATPase activity in 2N and DS fibroblasts after treating with or without AZD0530 demonstrated rescue of elevated lysosomal pH, v-ATPase activity deficits, and reduced lysosomal targeting of V1D (Fig. 6, B to E) in AZD0530-treated DS fibroblasts, which also exhibited lowered pY^{682}APP-βCTF (Fig. 6A). In addition, decreased interaction between V0a1 and APP-βCTF was also demonstrated in DS fibroblasts treated with AZD0530 (Fig. 6F).

To confirm the effects of lowering pY^{682}APP-βCTF by AZD0530 on the assembly of v-ATPase, siRNA constructs were used to knock down the expression of Fyn (fig. S8B). As expected, siFyn, but not siNC, substantially restored lysosomal acidification (Fig. 6G), v-ATPase activity (Fig. 6H), and lysosomal targeting of V1D (Fig. 6, K and L) in DS fibroblasts. Fyn knockdown also induced reassembly of disrupted V0/V1 complexes in DS fibroblasts (Fig. 6, I and J). Despite higher v-ATPase activity (Fig. 6H) and assembly (Fig. 6, I and J) in 2N cells, lysosomal pH was not lowered to an abnormal acidic range (Fig. 6G) consistent with the expectation that complementary regulatory systems, such as CLC-7 and additional proton

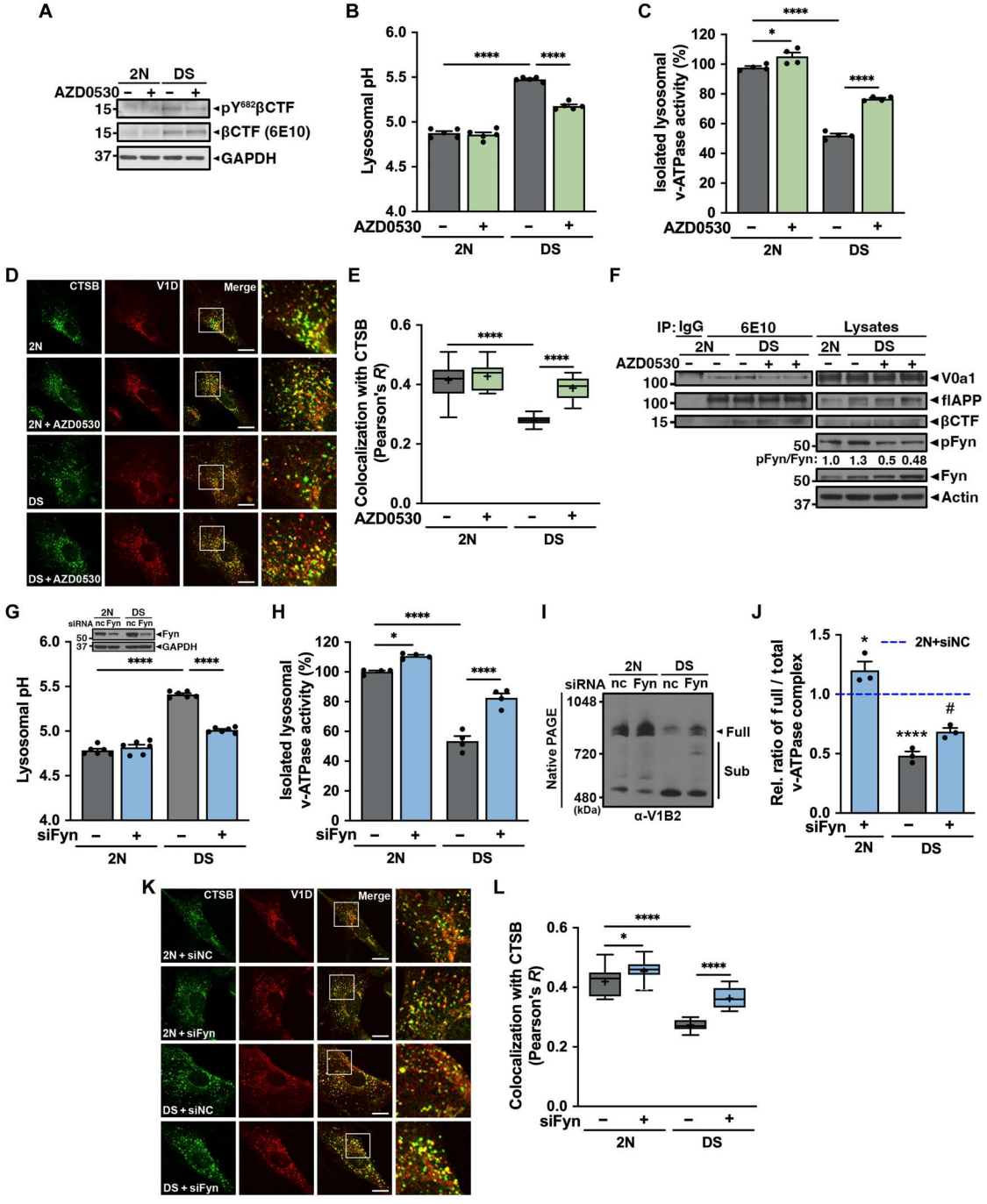

Fig. 6. Decreased levels of phosphorylated Tyr^{682} APP-βCTF rescues v-ATPase dysfunction in 2-year DS fibroblasts. (**A**) Immunoblots of phospho-Y^{682}APP-βCTF and APP-βCTFs distribution in total lysates of 2N and DS fibroblasts. (**B** and **C**) Lysosomal pH (C) ($n = 5$, five independent, triplicate) and ATP hydrolysis activity of v-ATPase using lysosomal fractions (D) ($n = 4$, four independent, triplicate) measured after treated with either DMSO (–) or 2 μM a Src family of nonreceptor tyrosine kinase inhibitor (AZD0530) for 24 hours. (**D** and **E**) Double-immunofluorescence labeling shows colocalization of V1D and CTSB in DMSO- or AZD0530-treated fibroblasts (D). Scale bar, 10 μm. Quantification shows colocalization in DMSO- or AZD0530-treated fibroblasts as calculated by Pearson's correlation coefficient ($n \geq 118$ cells, three independent) (E). (**F**) After treated with DMSO (–) or AZD0530 (+), cell lysates were IP with anti-APP (6E10) antibody, followed by IB with anti-V0a1 antibody. (**G** and **H**) Lysosomal pH (G) ($n = 6$, six independent, quadruplicate) and ATP hydrolysis activity of v-ATPase using lysosomal fractions (H) ($n = 4$, four independent, triplicate) measured after transfected with siRNA for either negative control (–) or 100 nM siFyn (+) for 48 hours. Immunoblot represents Fyn kinase protein levels. (**I**) Membrane fractions from siRNA transfected fibroblasts were resolved using the native PAGE. (**J**) The graph represents relative ratio of full complex divided by total complexes of v-ATPase. (**K** and **L**) Double-immunofluorescence labeling shows colocalization of V1D and CTSB in siRNA transfected fibroblasts (K). Scale bar, 10 μm. Quantification shows colocalization in siRNA transfected fibroblasts, as calculated by Pearson's correlation coefficient ($n \geq 139$ cells, three independent) (L). Quantitative data are presented as mean values with ±SEM, ordinary one-way ANOVA with Šidák's multiple comparisons test. Statistically significance between groups is shown by symbols: *2N versus others, #DS versus DS + AZD0530/siFyn. Each dot represents average value of technical replicates from each independent experiment.

leak channels (*14*), compensate for acute proton import changes to maintain optimal lysosomal pH. A lowering of pY^{682}APP-βCTF level below normal baseline would likely come into play not to lower pH below the normal range but to correct minor rises in lysosomal pH under physiological stress (or mild disease) conditions. Collectively, these data indicated that the dysfunction of v-ATPase in DS fibroblasts is likely mediated by elevated levels of pY^{682}APP-βCTF and that reducing its levels restores v-ATPase functioning.

v-ATPase dysfunction in DS model mice and human DS brain reflects impaired association of V0 and V1 sectors

We next extended our observations in vivo by investigating the possibility of similar lysosomal v-ATPase dysfunction and defective acidification in the Ts[Rb(12.17^{16})]2Cje (Ts2) mouse model of DS (*45*). Villar *et al.* identified and characterized Ts2 mice carrying a chromosomal rearrangement of the Ts65Dn genome. The Ts2 mouse expresses the same complement of trisomic genes as Ts65Dn and displays the same overt DS-related phenotype (*5*) but has the advantages of yielding male mice that are fertile (unlike Ts65Dn) and female mice that have higher trisomy transmission rates, resulting in an approximately three-fold higher viable offspring rate compared to that in Ts65Dn mice (*45*). Extensive published analyses have demonstrated that Ts2 exhibits an identical neurological phenotype to Ts65Dn, with indistinguishable AD-related pathological and synaptic plasticity abnormalities, changes in abnormal APP metabolism, age-dependent endosomal and cholinergic phenotypes, and timings of onset and progression of these anomalies (*46*–*48*).

To monitor lysosomal acidification in vivo, we crossed Ts2 mice with neuron-specific Thy1 promotor–driven transgenic mRFP-eGFP-LC3 (TRGL) mice to yield (Ts2xTRGL) mice as described previously (*13*). Introduction of a third fluorescence probe by immunocytochemical labeling with CTSD antibody allowed us to detect lysosomes and autolysosomes (ALs), and, based on their acidification state, to discriminate LC3-positive AL that had fused with lysosomes but had not properly acidified from LC3-positive, CTSD-negative autophagosomes. A computer-assisted unbiased measurement of hue angle (an index of wavelength) of individual triple fluorescent vesicles enabled a relative vesicle pH determination and objective assignment of vesicle identity (*13*). The confocal images were collected from neocortex sections of 8-to-9-month-old Ts2xTRGL and age-matched TRGL mice (Fig. 7A). In Ts2xTRGL mice, numbers of fully acidified AL (purple puncta) were decreased compared to that in control TRGL mice, whereas poorly acidified AL (white puncta) increased in number (Fig. 7B).

Next, to assess lysosomal v-ATPase activity in 8-to-9-month-old Ts2 and age-matched control (2N) mice, we performed biochemical fractionations to obtain Lyso fractions from the cortex of hemibrains using an iodixanol step gradient (fig. S9). WB analysis using various organelle markers identified Lyso within fractions 15 to 18 (fig. S9; Lyso), while measurements of the ATP-hydrolytic activity in this enriched lysosome fraction revealed a ~50% lowered ATP hydrolysis rate in the lysosomes from Ts2 mice relative to those in 2N control mice (Fig. 7C). While the TRGL probe assessed pH selectively in neurons, the v-ATPase assay assessed activity from all brain cell types, which are expected also to have a Ts2 phenotype in this systemic disorder.

We also performed WB analysis using iodixanol step gradient samples to investigate whether lysosomal targeting of v-ATPase subunits to lysosomes was also disrupted in Ts2 mice. V1 subunits in the Lyso (L+) fraction from Ts2 mouse brain were present at markedly decreased levels compared to those in 2N and were increased in other fractions (Lyso−; L−) (Fig. 7, D and E). V0 subunit levels in the Lyso fraction were not changed (Fig. 7, D and E), as expected from our experiments above. To confirm disruption of v-ATPase assembly in 8-to-9-month-old Ts2 mice, we performed native PAGE analysis using a membrane fraction from the cortex. Native PAGE analysis showed that the relative ratio of fully assembled v-ATPase divided by total v-ATPase (fully assembled v-ATPase plus subcomplexes of v-ATPase) was significantly reduced in the Ts2 mouse, compared with 2N (Fig. 7, F and G). We additionally observed disruption of v-ATPase assembly in the membrane fraction from frozen brain from individuals with DS, which showed increased levels of flAPP and APP-βCTF (fig. S10), compared to the control group (Fig. 7, H and I).

Lysosomal dysfunction in DS model mice is reversed by lowering elevated pY^{682} APP-βCTF levels

In further investigations, we showed that the level of pY^{682}APP-βCTF, measured with Tyr phosphorylation specific antibodies, is nearly twofold higher in cortex of 8-to-9-month-old Ts2 mouse brain by WB analysis (Fig. 8, A and B). To determine the effects of raised levels of pY^{682}APP-βCTF, in vivo, we then treated Ts2 mice with vehicle or AZD0530 (5 mg/kg per day) by oral gavage for 4 weeks (*49*). We confirmed by WB analysis that AZD0530 decreased pY^{682}APP-βCTF levels in cortex from 8-to-9-month-old Ts2 mice in vivo (Fig. 8, C and D) and significantly rescued abnormal lysosomal acidification (Fig. 8, E and F) compared to vehicle-treated (Veh) mice and restored v-ATPase activity (Fig. 8G). In addition, the lowered level of pY^{682}APP-βCTF in Ts2 mice restored the normal ratio of full versus total v-ATPase complex in Ts2 mouse brain (Fig. 8, H and I) and increased association of V1 subunits in Lyso fractions (Fig. 8, J and K). Notably, supporting our foregoing evidence in fibroblasts for tonic modulation of v-ATPase, the lowered pY^{682}APP-βCTF levels in wild-type (WT) mice induced supranormal levels of v-ATPase activity and proportions of fully assembled v-ATPase complex in enriched lysosome fractions and an increased proportion of V1 subunits associated with the V0 sector on lysosomes.

The foregoing results establish lysosomal v-ATPase dysfunction in DS model brain in vivo as well as in authentic DS in fibroblasts from individuals with DS. We also demonstrate its further dependence on Tyr^{682} phosphorylation of APP in DS.

v-ATPase deficits are associated with pY^{682}APP-βCTF in APP-based mouse models of AD

As an initial extension of our findings in DS to early onset AD models induced by *hAPP* overexpression or *APP/PSEN1* mutations, we investigated the relevance of Tyr^{682}APP phosphorylation to defective lysosomal acidification and function in female AD mouse models, which show greater histopathology than males (*50*, *51*): 6-month-old 5xFAD mice exhibiting early-onset amyloidosis (at 2 months) and 6-month-old Tg2576 mice with a later age of onset of amyloidosis (at 10 to 12 months). v-ATPase activity measured in Lyso fractions was reduced by ~45% in each model relative to WT controls (Fig. 9, A and F). Phosphorylation of APP at Tyr^{682} is increased in AD brain (*38*, *39*, *44*). Accordingly, we found levels of pY^{682}APP-βCTF to average nearly threefold higher in Tg2576

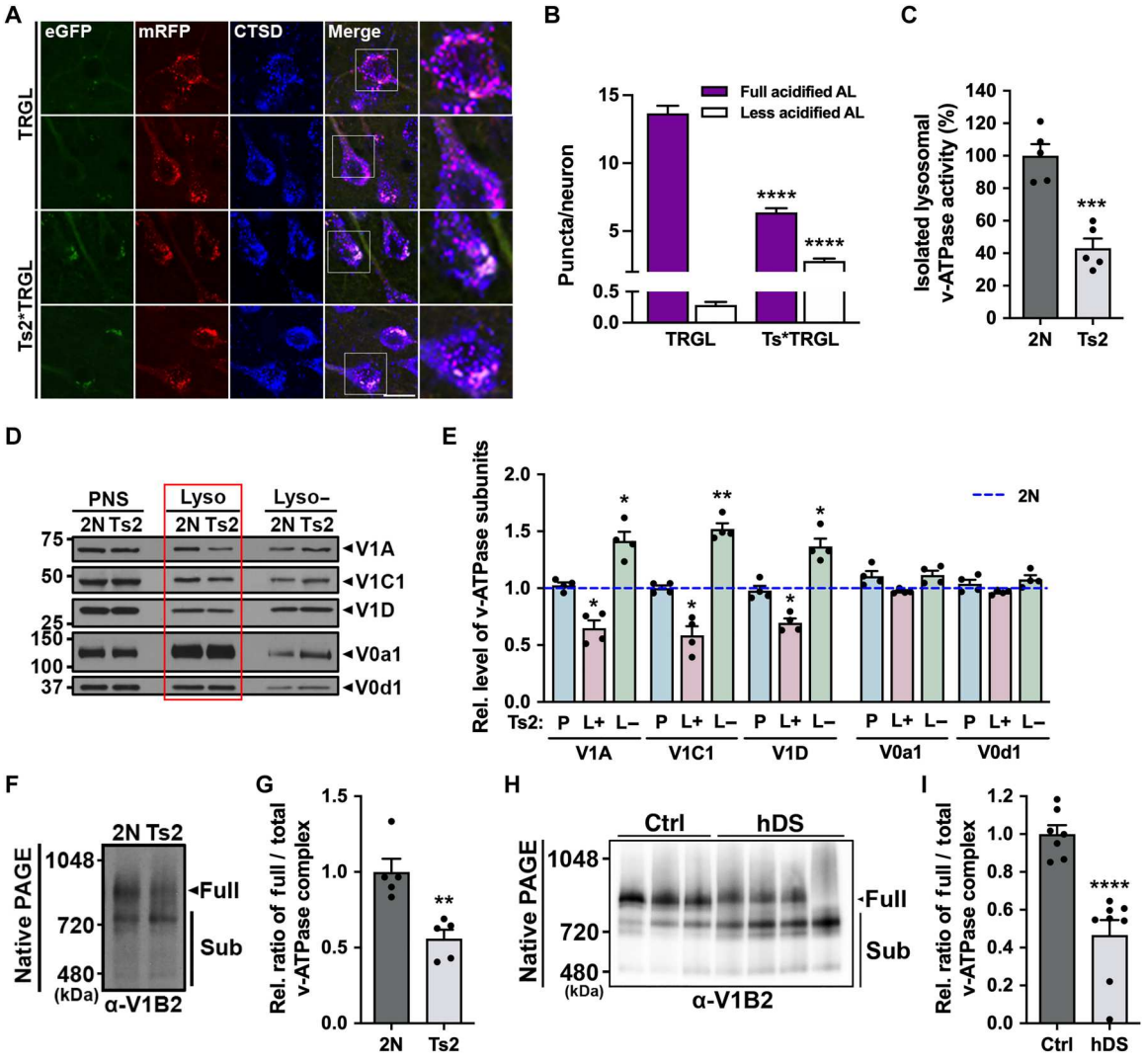

Fig. 7. Defective lysosomal v-ATPase function in Ts2 mouse model and human DS brain. (**A** and **B**) Representative fluorescence images of tfLC3 color changes of TRGL or Ts2xTRGL adult brain (A) and respective quantification of puncta representing ALs (fully or less acidified) (B). For data analysis, color change of tfLC3-positive vesicles was calculated with CTSD colabeling. Bar colors denote the colors of puncta; purple bars indicate tfLC3 with CTSD (fully acidified ALs, quenched eGFP), and white bars indicate tfLC3 with CTSD (less acidified ALs, unquenched eGFP) (n = 504 neurons, 6 TRGL mice; n = 537 neurons, 6 Ts2xTRGL mice). (**C**) ATP hydrolysis activity of v-ATPase was measured using Lyso fraction (15 to 18) of the iodixanol step gradient from adult mice (n = 5, triplicate). (**D**) Adult mouse brain from control (2N) and Ts2 homogenates were fractionated through an iodixanol step gradient. Each fraction [lysosomal enriched fraction (Lyso): 15 to 18; exclude lysosomal enriched fraction (Lyso−): 1 to 14 and 19 to 22] and post-nuclear supernatant (PNS) were resolved using the SDS-PAGE and immunoblotted with anti-V1A, anti-V1C1, anti-V1D, anti-V0a1, and anti-V0d1 antibodies. (**E**) The graphs represent levels of v-ATPase subunits from each fraction (n = 4). (**F** and **H**) Membrane fractions from mouse brain (F) or frozen human brain tissue (H) were resolved using the native. (**G** and **I**) The graph represents relative ratio of full complex divided by total (full plus partial complexes) complexes of v-ATPase (n = 5). Quantitative data (B, C, E, G, and I) are presented as mean values with ±SEM, two-tailed unpaired t test (C, G, and I) and ordinary one-way ANOVA with Šidák's multiple comparisons test (B and E). Each dot corresponds to average value of technical replicates from one mouse.

mouse brain (Fig. 9, B and C). To confirm disruption of v-ATPase assembly in Tg2576 mouse, we performed native PAGE analysis using membrane fractions from cortex. Native PAGE analysis showed that the relative ratio of fully assembled v-ATPase divided by total v-ATPase complex was significantly reduced in the Tg2576 mouse, compared with WT (Fig. 9, D and E). We observed similar results in brains of the 5xFAD mouse model of AD (Fig. 9, F to J).

DISCUSSION

In all forms of AD, the impaired clearance of autophagic and endocytic substrates by lysosomes causes profuse accumulations of neuronal waste, including the buildup in lysosomes of key APP metabolites (e.g., APP-βCTF and Aβ), ultimately leading to lysosomal membrane permeability and neuronal cell death (*26*, *52*–*54*). Here, we have established a primary APP-dependent mechanism underlying lysosome dysfunction in DS, a congenital genetic disorder responsible for the most prevalent form of early onset AD (*55*–*57*). Lysosomal v-ATPase function is disrupted by APP-βCTF

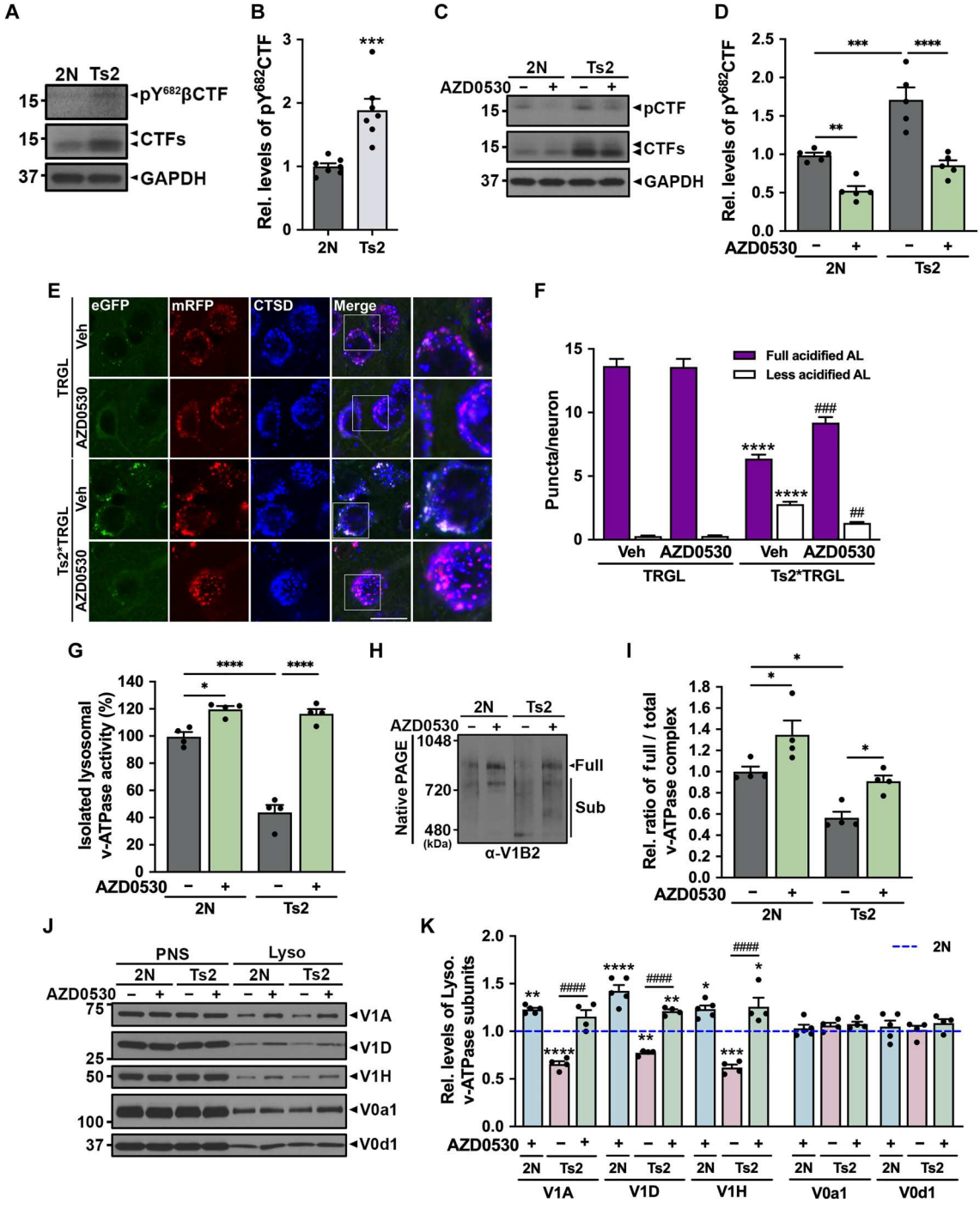

Fig. 8. Reduction in levels of phosphorylated Tyr^{682} APP-βCTF in vivo reverses v-ATPase dysfunction in brains of DS model mice. (**A** and **B**) Immunoblot (A) and the graphs (B) represent pY^{682}APP-βCTF and CTFs levels in mouse brain (n = 7). (**C** and **D**) Immunoblot (C) and the graphs (D) represents pY^{682}APP-βCTF and CTFs levels after treated with either vehicle (−) or AZD0530 (+) for 4 weeks (n = 5). GAPDH served as a loading control. (**E** and **F**) Representative fluorescence images of tfLC3 color changes of adult brain after treatment with vehicle (Veh) or AZD0530 for 3 weeks (E) and respective quantification of puncta representing ALs (fully or less acidified) (n = 452 neurons, 4 TRGL; n = 491 neurons, 4 AZD0530-treated TRGL; n = 476 neurons, 4 Ts2xTRGL; n = 484 neurons 4 AZD0530-treated Ts2xTRGL) (F). (**G**) ATP hydrolysis activity of v-ATPase measured using Lyso fraction (15 to 18) of iodixanol step gradient from adult mouse brain after treatment with vehicle (−) or AZD0530 (+) for 4 weeks (n = 4). (**H**) Membrane fractions from AZD0530-treated adult mouse brain were resolved using native PAGE. (**I**) The graph represents relative ratio of full complex divided by total (full plus partial complexes) complexes of v-ATPase (n = 4). (**J**) Homogenates from AZD0530-treated adult mice brain were fractionated through an iodixanol step gradient. The Lyso fraction and the PNS were immunoblotted using indicated antibodies. (**K**) The graphs represent levels of lysosomal v-ATPase subunits (n = 5 TRGL; n = 4 Ts2xTRGL; n = 4 AZD0530-treated Ts2xTRGL). Quantitative data are presented as mean values with ±SEM, two-tailed unpaired t test (B) and ordinary one-way ANOVA with Šidák's multiple comparisons test (D, F, G, I, and K). Statistically significance between groups is shown by symbols: *2N + Veh versus others, #DS + Veh versus DS + AZD0530. Each dot corresponds to average value of technical replicates from one mouse.

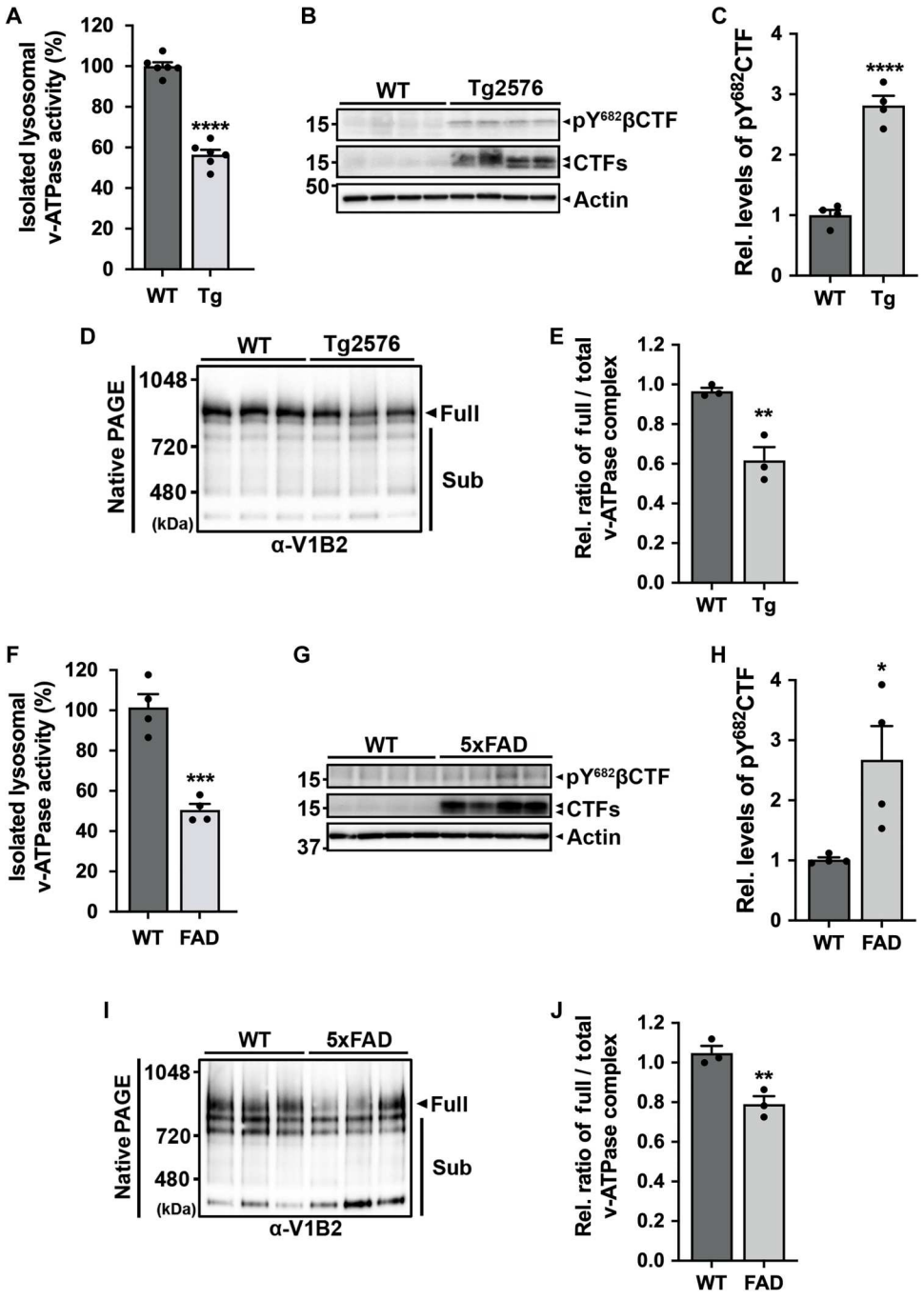

Fig. 9. Defective v-ATPase dysfunction in APP-based AD model mouse. (**A**) Lysosomal v-ATPase activity measured colorimetrically as ATP hydrolysis with and without ConA. Activity assays were performed on lysosomal enriched fraction (15 to 18) of iodixanol step gradient from 6-month Tg2576 female adult brain pretreated with *o*-vanadate to minimize nonspecific ATPase activity ($n = 6$, triplicate). (**B**) Immunoblot represents pY^{682}APP-CTFs and APP-CTFs protein levels in 6-month female Tg2576. Actin served as a loading control. (**C**) The graph shows relative band intensity of pY^{682}APP-βCTF proteins ($n = 4$). (**D**) Membrane fractions from 6-month Tg2576 female adult brain were resolved using the native PAGE and immunoblotted with anti-V1B2 antibody. (**E**) The graph represents relative ratio of full complex divided by total (full plus partial complexes) complexes of v-ATPase ($n = 3$). (**F**) Lysosomal v-ATPase activity measured colorimetrically as ATP hydrolysis with and without ConA. Activity assays were performed on lysosomal enriched fraction (15 to 18) of iodixanol step gradient from 6-month 5xFAD female adult brain pretreated with *o*-vanadate to minimize nonspecific ATPase activity ($n = 4$, triplicate). (**G**) Immunoblot represents pY^{682}APP-CTFs and APP-CTFs protein levels in 6-month female 5xFAD. (**H**) The graphs show band intensity of pY^{682}APP-βCTF protein ($n = 4$). (**I**) Membrane fractions gradient from 6-month 5xFAD female adult brain were resolved using the native PAGE and immunoblotted with anti-V1B2 antibody. (**J**) The graph represents relative ratio of full complex divided by total (full plus partial complexes) complexes of v-ATPase ($n = 3$). Quantitative data (A, C, E, F, H, and J) are presented as mean values with ±SEM, two-tailed unpaired *t* test. Each dot corresponds to average value of technical replicates from one mouse.

directly interacting with the critical membrane-anchored V0a1 subunit of v-ATPase, thereby impeding assembly of the complete V1 sector with the V0 sector of v-ATPase. The relevance of this molecular interaction is supported by a previous unbiased analysis of the synaptosome interactome of the AICD harboring the conserved YENPTY region of interest. This analysis revealed V0a1 and V0d1 and various V1 subunits to be AICD interactome members (*33*). Reinforcing the pathogenic importance of the APP-βCTF interaction with V0a1 subunit, mutations of *PSEN1*, a major cause of early-onset AD (*58*), are also known to disrupt PSEN1 holoprotein endoplasmic reticulum chaperone role in facilitating V0a1 glycosylation, folding, and stability, thereby impeding adequate delivery of the key subunit to lysosomes (*25*, *59*). Further highlighting V0a1 as a common disease target in AD, other evidence suggests that V0a1 subunit dysfunction is compromised in additional neurodegenerative conditions featuring prominent lysosomal dysfunction, including LRRK2-linked PD (*60*) and the lysosomal storage disorder, CLN1 (*61*).

We further establish here that Tyr^{682} APP phosphorylation confers selectivity to the pathogenic interaction of pY^{682}APP-βCTF with V0a1 using molecular modeling and docking studies. While planned for future analysis, additional confirmation by establishing direct interaction using biochemical methods is beyond the scope of the present study. Among the challenges necessitating extensive biophysical analysis in a full study are complexities in preserving and ensuring proper V0a1 conformation within a membrane after isolation and sensitively detecting bound APP-βCTF peptide by mass spectroscopy. Notwithstanding this limitation, our collective results firmly establish the role of APP-βCTF in selectively binding and disrupting the v-ATPase complex and its activity. Moreover, the modestly elevated level of endogenous APP-βCTF in DS (*62*) is necessary and sufficient to raise lysosomal pH and partially inactivate lysosomal enzymes, as these pathological consequences are reversed by reducing APP-βCTF levels (*5*) either directly or via BACE1 inhibition, which also lowers pY^{682}APP-βCTF levels. Alternatively, reversal could also be achieved by inhibiting the activity of tyrosine kinases, which targets Tyr^{682} on APP (*63*–*65*) and is overactive in DS. While other genes in the trisomic chromosomal region in DS fibroblasts and Ts2 mice may have additional influence on lysosomal function, we show that elevated levels of pY^{682}APP-βCTF in AD mouse models, which lack the trisomy of DS, induce the same lysosomal acidification deficit as in DS models.

We found inhibition of Fyn activation to be a contributing factor in lowering pY^{682}APP-βCTF levels in DS, consistent with other studies in DS and AD (*39*, *66*). We do not contend, however, that Fyn is the only possibly relevant kinase involved in all lysosomal pH-related disease contexts or even that overactivation of tyrosine kinase is essential to the mechanism of v-ATPase deficiency operating in AD. Tyr^{682} APP phosphorylation is a constitutive process, so a proportion of APP and βCTF molecules normally contains Tyr^{682} phosphate, as we have shown. Levels of pY^{682}APP-βCTF may therefore become elevated without overactivating any particular tyrosine kinase if (i) β-cleavage of APP is accelerated (e.g., many AD-related factors that activate BACE1); (ii) conversion of APP-βCTF to Aβ is inhibited (e.g., PSEN1/2 loss of function or inhibition); or (iii) APP-βCTF is induced to accumulate in lysosomes (e.g., cathepsin inhibition in various disease contexts). In our study, we used an inhibitor with high affinity for Fyn kinase as a tool to suppress Tyr^{682} phosphorylation to provide proof of principle that lowering levels of pY^{682}APP-βCTF, regardless of the specific cause of an abnormal elevation, can ameliorate v-ATPase dysfunction.

The pathogenic binding to v-ATPase is an effect of APP-βCTF, but not Aβ or APP-αCTF, based on our use of γ- and α-secretase inhibitors and peptide competition assays with v-ATPase subunits. Brain levels of APP-βCTF are not only elevated in DS but also in individuals with familial AD (FAD) caused by APP or PSEN1 mutations (*5*, *29*, *67*, *68*) and in induced pluripotent stem cells derived from homozygous APOE4 carriers (*69*). Steady-state levels of APP-βCTF likely underestimate its production and flux through the endosomal-lysosomal system when APP endocytosis rates are elevated, as is likely in AD and DS. In DS, expression of the AD phenotype of endosomal and lysosomal anomalies (*5*, *29*, *68*) is dependent on a single extra copy of APP, highlighting the sensitivity of the v-ATPase system response to modest APP-βCTF elevations. Levels of pY^{682}APP-βCTF in brain are also elevated in individuals with late-onset "sporadic" AD (*38*, *39*) as well as in two different AD model mice (Tg2576 and 5xFAD).

The foregoing mechanism of v-ATPase impairment in FAD/DS is potentially relevant to explaining the similar lysosomal dysfunction in sporadic AD. In late-onset (sporadic) AD, APP-βCTF elevation, in the absence of a rise in APP levels, results from potentially multiple factors that may be additive. These include an increased level of BACE1 activity (*70*, *71*), cell stress–activated Tyr^{682} APP phosphorylation, which notably also promotes β-cleavage of APP over α-cleavage (*72*), and APP processing regulation by Genome-wide association studies (GWAS) identified AD risk genes such as BIN1, SORL1, ABCA7, and RIN3 (*73*, *74*). In addition, as hydrolytic efficiency declines in aging due to rising oxidative stress, lipid accumulations, and other aging factors (*75*–*77*), APP-βCTF may well build up in lysosomes disproportionately to flAPP levels (*78*, *79*) and inhibit v-ATPase.

Besides regulating substrate hydrolysis, the intraluminal pH of lysosomes modulates diverse signaling functions including maturation of lysosomal hydrolases (*80*), modification of certain cargoes delivery to lysosome (*81*, *82*), fusion of lysosomes with other organelles/cell surface (*83*, *84*), and retrograde axonal transport of LAMP-positive compartments (*85*). Therefore, v-ATPase activity is increasing recognized to be tightly regulated (*21*, *86*). Varied factors modulate V1 sector association with the V0 sector (*24*) and reversible association of specific individual V1 subunits with the complex may also have modulatory effects on activity (*17*, *87*). The regulatory factors are best characterized in yeast (*17*, *18*, *86*) although several factors have been reported in mammals (*88*–*90*). Given the diverse biological roles of v-ATPase and luminal pH regulation, it is not unexpected to find global effects of loss of function mutations of v-ATPase in various diseases, especially those with prominent neurodegenerative phenotypes (*24*). The association of early lysosome acidification failure in AD models with a cascade of autophagic and neurodegenerative phenomena underlying β amyloidosis and lysosomal cell death has been recently described (*26*).

Although not the main focus of our analyses on APP-βCTF pathogenicity in AD, we observed consistently that manipulations lowering pY^{682}APP-βCTF below normal baseline induced supranormal v-ATPase assembly, lysosomal ATPase activity, and acidification. Such conditions included knockdown of APP (Fig. 2), BACE1 inhibitor treatment (Fig. 3), and reducing levels of tyrosine

kinase activity (Figs. 6 and 8). Collectively, these findings support the possibility that change in APP-βCTF levels in normal lysosomes under varying physiological levels may tonically modulate v-ATPase activity, although implications of such potential modulation, including therapeutic applications, require future investigation.

In conclusion, *APP* joins *PSEN1* as not only the major monogenic causes of early-onset AD but as genes directly responsible for extreme disruption of lysosomal function and autophagy that is evident in essentially all forms of AD (*91*) and shown to be the catalyst and driver for varied downstream pathophysiology associated with AD development (*26*, *92*, *93*). Our results unequivocally establish the importance of APP-βCTF in AD etiology by demonstrating a direct pathogenic action of APP-βCTF in the context of DS and AD. Together with other emerging data, our findings point toward acidification failure within the lysosomal network as a potential unifying pathogenic mechanism in AD, driven by converging genetic, aging, and environmental factors of varying influence depending on the subtype of AD (*24*, *75*, *77*). Last, mounting preclinical evidence establishes the ameliorative impact of lysosome re-acidification not only on lysosomal efficacy but on neuropathological signatures, synaptic plasticity, and cognition. Hence, acidification rescue represents a promising innovative target for the remediation of lysosome dysfunction in AD and related disorders (*94*–*96*).

MATERIALS AND METHODS

Materials

Materials are provided in table S2.

Cell lines and transfection

Human foreskin fibroblasts from male patient with DS (DS) and male diploid age-matched controls (2N) were purchased from the Coriell Institute for Medical Research (2-year-old: AG06922 and AG07095; 5-month-old: AG07096 and GM08680) and maintained according to the distributor′s protocols (www.coriell.org/). Throughout this study, fibroblasts were used below passage number 15 to keep the original character and morphology.

siRNA against human APP and negative control DsiRNA were purchased from Integrated DNA Technologies (IDT) and used as previously described (*31*). siRNA against human Fyn was purchased from Life Technologies Corp. Cells were transfected using Lipofectamine RNAiMAX according to the manufacturer′s protocol.

pcDNA-APP-βCTF was previously described (*31*). Cells were transiently transfected using Lipofectamine 2000 according to the manufacturer′s protocol.

Animals

All animal procedures were performed following the National Institutes of Health Guidelines for the Humane Treatment of Animals, with approval from the Institutional Animal Care and Use Committee at the Nathan Kline Institute for Psychiatric Research. Four mouse models were used: (i) Control mice (2N), C57BL/6JEi × C3H/HeSnJ; (ii) Ts[Rb(12.17^{16})]2Cje (Ts2), carrying a chromosomal rearrangement of the Ts65Dn genome whereby the marker chromosome has been translocated to Chromosome 12 (MMU12) forming a Robertsonian chromosome (*45*), were studied at 8 to 9 months; (iii) TRGL (Thy1 mRFP-eGFP-LC3), expressing tandem fluorescent mRFP-eGFP-LC3 under individual Thy 1 promoters (*13*); (iv) Ts2 × TRGL, a transgenic Ts2 mouse model expressing tandem-fluorescent mRFP-eGFP-LC3 under individual Thy1 promoters, were studied at 8 to 9 months; (v) 5xFAD × TRGL, 5xFAD (Tg6799, C57BL/6NTAC), which express mutant human APP and PSEN1 (APP KM670/671NL: Swedish, I716V: Florida, V717I: London, PSEN1 M146L, L286V), were crossed with TRGL and were studied at 6 months together with age-matched controls; (vi) Tg2576 (B6;SJF, Tg(APPSWE)2576Kha), expressing mutant human APP (Swedish K670N/M671L), were studied at 6 months together with age-matched controls. All mice were genotyped by PCR. Mice were group-housed under 12 hour light/dark cycle at constant room temperature and provided with food and water ad libitum. Age-matched WT mice of comparable background were used as controls. The samples were not blinded during initial planning of animal selection because we wanted to ensure that the number of WT and pathogenic mouse models were balanced and age and sex were matched. The mice were then randomly assorted for the studies and the investigators were blinded when doing the experiments and running data analyses.

Ts2 × TRGL mouse generation

For the generation Ts2 x TRGL mice, Ts2 mice were bred with our previously described TRGL (***T****hy1* m**R**FP-e**G**FP-**L**C3) transgenic mice expressing tandem fluorescent mRFP-eGFP-LC3 (*13*). Ts2xTRGL mice were studied at 8 to 9 months together with age-matched controls. Mice used in this study were maintained according to Institutional Animal Care and Use Committee guidelines and protocols (AP2022-718) for animal experimentation at Nathan S. Kline Institute.

Human individual details

Postmortem frozen brain tissues (Brodmann area 9) from human DS and control individuals (table S3) were provided by the Brain and Tissue Bank Department, Department of Developmental Neurobiology, New York State Institute for Basic Research in Developmental Disabilities, Staten Island, NY. This study was performed by using anonymous coded tissue samples without any donor identifiers.

Analysis of AL acidity of TRGL mouse and vesicle quantification

Immunohistochemistry was performed as previously described (*25*). Animals were anesthetized with a mixture of ketamine (100 mg/kg body weight) and xylazine (10 mg/kg body weight) and intracardially perfused by 0.9% saline. Brains were dissected and immersed in the same fixative for 24 hours, and then 40 μm sagittal sections were made using a vibratome. Immediately after sectioning, sections were immunolabeled with the indicated antibodies overnight and then visualized with Alexa Fluor–conjugated secondary antibodies. Imaging was performed using a plan-Apochromat 40×/1.4 oil objective lens on a LSM880 laser scanning confocal microscope. The three colors (RGB; red, green, blue) intensity of each vesicle were calculated by Zen from Carl Zeiss Microscopy using the profile function. The R, G, and B ratio of each vesicle was calculated into a hue angle and saturation range by following formula: Hue° = IF{180/PI()*ATAN2[2*R-G-B,SQRT(3)*(G-B)] < 0,180/PI()*ATAN2[2*R-G-B,SQRT(3)*(G-B)] + 360,180/PI()*ATAN2[2*R-G-B,SQRT(3)* (G-B)]}. Saturation percent of the hue angle was calculated by entering the values of R,

G, and B for a given puncta into the following formula = [MAX(RGB)-MIN(RGB)]/SUM[MAX(RGB) + MIN(RGB)]*100, provided lightness is less than 1, which is the usual case for our data. Vesicle quantification was performed as previously described (*13*).

Saracatinib pharmacokinetics

To examine the effect of a Src family of nonreceptor tyrosine kinase inhibitor (saracatinib; AZD0530) in a preclinical DS mouse model, mice received a dose of 5 mg/kg per day administered orally twice daily for 3 to 4 weeks.

Lysosomal pH measurement

Following the addition of 250 μg of LysoSensor Yellow/Blue dextran treatments, cells were incubated for 24 hours. The samples were then read in a Wallac Victor 2 fluorimeter (PerkinElmer) with an excitation at 355 nm. The ratio of emission 440 nm/535 nm was then calculated for each sample. The pH values were determined from the standard curve generated via pH calibration samples. To measure lysosomal pH in presence of peptide, we directly added 5 μM peptide to the cells for 24 hours at 37°C, wash out the peptide containing medium (three times), and then added 250 μg of LysoSensor Yellow/Blue dextran for 24 hours at 37°C.

Lysosomal isolation

Cells were incubated in growth medium containing 10% dextran-conjugated magnetite (DexoMAG 40) for 24 hours and then changed in normal growth media for 24 hours. Cells were washed with 1× phosphate-buffered saline (PBS) and then harvested in 4 ml of ice-cold buffer A [1 mM Hepes (pH 7.2), 15 mM KCl, 1.5 mM MgAc, 1 mM dithiothreitol (DTT), and 1× protease inhibitor cocktail (PIC)]. Cells were then homogenized with 40 strokes of a loose-fitting pestle in a Dounce homogenizer and then passed through a 23 G needle five times. After homogenization, 500 μl of ice-cold buffer B [220 mM Hepes (pH 7.2), 375 mM KCl, 22.5 mM MgAc, 1 mM DTT, and 20 μM deoxyribonuclease I (DNase I)] was added, and samples were then centrifuged at 750*g* for 10 min. The supernatant was then decanted over a QuadroMACS LS column (Miltenyi Biotec, 130-042-976) that had previously been equilibrated with 0.5% bovine serum albumin (BSA) in PBS, and then collected non-lysosomal fraction (Flow) to flow through via gravity. The pellet was subjected to re-addition of 4 ml of ice-cold buffer A, 500 μl of ice-cold buffer B and then resuspended and recentrifuged. This second supernatant was also passed over the column and allowed to flow through via gravity. DNase I (10 μl/ml in PBS) was added, and the column was then incubated for 10 min and washed with 1 ml of ice-cold PBS. Lysosomes were eluted by removing the column from the magnetic assembly, adding 100 μl of PBS for immunoblotting / M1 buffer [10 mM tris (pH 7.5), 250 mM sucrose, 150 mM KCl, 3 mM β-mercaptoethanol, and 20 mM $CaCl_2$] for v-ATPase activity and proton translocation assay and forced through the column using a plunger. For the co-IP assay, lysosomes were r-suspended in 1× NativePAGE sample buffer with 1% Digitonin. After incubation on ice for 30 min, the resolved samples centrifuged at 20,000*g* for 30 min and then collected lysosomes including solubilized native proteins. Fresh lysosomes (100 μg) were pulled down with C1/6.1 antibody for 24 hours at 4°C with gentle rotation.

v-ATPase activity assay

Lysosome-enriched fractions (fibroblasts: 4 μg; mouse brain: mixture of 20 μl each Optiprep fraction from 15 to 18) were mixed with 0.052% NaN_3, which is an inhibitor of P- and F-type ATPase, to minimize nonspecific ATPase activity. The v-ATPase activity measured using an ATPase assay kit according to the manufacturer′s protocol. Control samples were measured in the presence of the v-ATPase inhibitor ConA (1 μM), and the experimental values were subtracted accordingly. Absorbance was measured at 650 nm, and solutions of P_i were used to generate a standard curve.

Proton translocation assay

Proton transport activity into the lumen of isolated lysosomes was measured by fluorescence quenching of ACMA in the presence or absence of 1 μM ConA. Lysosome-enriched fractions (25 μg) were added to a cuvette containing 2 ml of reaction buffer [10 mM Bis-TrisPropene [BTP]-MES (pH 7.0), 25 mM KCl, 2 mM $MgSO_4$, 10% glycerol, and 2 μM ACMA]. The reaction was started by the addition of 1 mM ATP in BTP, pH 7.5, a measurement (Ex412/Em480) taken every 5 s for 600 s on a SpectraMax M5 multimode reader (Molecular Devices).

Subcellular fractionation

For fibroblasts, cells were washed and harvested with 1× PBS and then resuspended in ice-cold membrane preparation buffer [5 mM tris (pH 7.4), 250 mM Sucrose, 1 mM EGTA, and 1× PIC]. Cells were then briefly homogenized and then passed through a 26 G needle 10 times. For mouse brain, half of an adult mouse brain was homogenized in 10× volume homogenization buffer [HB; 250 mM sucrose, 10 mM tris-HCl (pH 7.4), 1 mM EDTA, and protease and phosphatase inhibitors] by 40 strokes in a Teflon-coated pestle. For human brain, the frozen brain tissue (frontal cortex, Brodmann Area 9; table S3) was homogenized in 10× volume HB by three strokes (20 s each, with a 10 s pause in between) of an automatic homogenizer. After 10 min on ice, samples were then centrifuged at 1000*g* for 10 min. The supernatants were fractionated into cytosolic and membrane fractions by high-speed centrifugation at 150,000*g* for 60 min. The membrane fractions (pellet after centrifugation) lysis with 100 μl of lysis buffer [10 mM tris (pH 7.4), 150 mM NaCl, 1 mM EDTA, 1 mM EGTA, 1% Triton X-100, and 0.5% NP-40) and sonication for immunoblotting.

Iodixanol step gradient

Half of an adult mouse brain was homogenized in 10× volume HB by 40 strokes in a Teflon-coated pestle. Lysates were centrifuged at 1000*g* for 20 min to generate the post nuclear supernatant (PNS). The PNS was then adjusted to 25% OptiPrep with 50% OptiPrep in HB. The resulting mixture, 2 ml in 25% OptiPrep, was placed at the bottom of a clear ultracentrifuge tube and was overlaid successively with 1.5 ml each of 20, 15, 14, 12.5, 10, and 5% OptiPrep in cold HB. The gradients were centrifuged for 18 hours at 100,000*g* at 4°C in an SW 40 rotor (Beckman Coulter). Fractions (500 μl) were collected from the top of the ultracentrifuge tubes and analyzed by WB analysis.

Gel electrophoresis and immunoblotting

Samples were mixed with 2× urea sample buffer (9.6% SDS, 4 M urea, 16% sucrose, 0.005% bromophenol blue [BPB], and 4.6% β-

mercaptoethanol) and incubated 15 min at 55°C for V0 subunits of v-ATPase electrophoresis, otherwise samples mixed with 1× SDS sample buffer [62.5 mM tris (pH 6.8), 10% glycerol, 1% SDS, 20 mM DTT, 5% β-mercaptoethanol, and 0.005% BPB] and incubated 5 min at 100°C followed by electrophoresis on Novex 4 to 20% Tris-Glycine gradient gels (Invitrogen, WXP42020BOX; WXP42026BOX). Proteins were transferred onto 0.2 μm nitrocellulose membranes (Pall Laboratory, p/n 66485), and the membrane was blocked using 5% nonfat milk or 5% BSA for detecting phosphoproteins. The membrane was then incubated overnight in primary antibody followed by incubation with horseradish peroxidase–conjugated secondary antibody. The blot was developed using ECL kits.

Co-immunoprecipitation

Proteins were prepared from cells using an ULTRARIPA kit for Lipid Raft, which can efficiently and rapidly extract membrane proteins/membrane-associated proteins enriched in lipid rafts with native structure and native function, according to the manufacturer′s protocol. Cell lysates were pulled down with proper antibodies for 24 hours at 4°C with gentle rotation. The mixture was then incubated with 30 μl of Protein A/G Mix Magnetic Beads and washed with lysis buffer and Magnetic Stand. The samples were dissociated by 2× urea sample buffer. For the peptide competition assay, 500 μg of fresh cell lysates was pulled down with C1/6.1 antibody in the presence of varying amounts of each peptide for 24 hours at 4°C with gentle rotation to minimize nonspecific binding.

Native gel immunoblot analysis

The pellet from the cell membrane fraction was resolved with 1% digitonin and 1× NativePAGE sample buffer, incubated on ice for 30 min, and then centrifuged at 20,000*g* for 30 min. Sample (15 μg) was mixed with 1% NativePAGE G-250 sample additive followed by electrophoresis on NativePAGE Novex 4-16% Bis-Tris Gels in 1X NativePAGE Running Buffer and then transfer using 1× NuPAGE Transfer buffer and 0.45 μm polyvinylidene difluoride membranes (Millipore, IPVH00010) according to the manufacturer′s protocol.

Confocal fluorescence microscopy

Cells were fixed with 4% paraformaldehyde (PFA) for 20 min, blocked with 5% horse serum, incubated with anti-CTSB goat pAb (CTSB; 1/250) for lysosomal marker and anti-V1D rabbit mAb (1/100) overnight at 4°C, followed by fluorescence-tagged secondary antibodies: donkey anti-Goat Alexa Fluor 488 (1/500) and goat anti-Rabbit Alexa Fluor 568 (1/500). Cells were imaged using a plan-Apochromat 40×/1.4 oil differential interference contrast objective lens on the laser scanning confocal microscope, LSM 510 META, with LSM software v3.5 (Carl Zeiss MicroImage Inc). Images were analyzed using ImageJ program (National Institutes of Health). Colocalization was determined using the Coloc 2 analysis tool on ImageJ software.

Proximity ligation assay

PLAs were performed according to the manufacturer′s protocol using the following reagents in the Duolink In Situ Detection Reagents Red kit. In brief, cells were plated on coverslips at a concentration of 10^5/ml. Cells were fixed using 4% PFA in PBS for 15 min and then permeabilized using 0.01% Triton X-100 in PBS for 20 min at room temperature. All subsequent incubations were performed at 37°C in a humid chamber. Nonspecific binding was minimized with the manufacturer′s blocking buffer for 30 min. Cells were incubated with primary anti-APP (C1/6.1) mouse (1/100) and anti-V0a1 rabbit mAb (1/100) overnight at 4°C and washed with buffer A (twice, 5 min). Coverslips were incubated with ligation mix for 30 min, washed twice with buffer A, and incubated with amplification mix. Coverslips were then washed with provided Buffer B twice (10 min), followed by 1 min washing with 0.01× Wash Buffer B. The samples were mounted with Duolink In Situ Mounting Medium with 4′,6-diamidino-2-phenylindole in the dark for 15 min at room temperature. The images were taken using a Zeiss LSM880 laser scanning confocal microscope at 20× objective lens. The number of signals per cell were analyzed using ImageJ program and then normalized to the protein levels.

MS analysis

The stained protein gel regions (fig. S2A, bands 1 to 6) were excised, and in-gel digestion was performed overnight with MS-grade trypsin at 5 ng/μl in 50 mM NH_4HCO_3 digest buffer. After acidification with 10% formic acid, peptides were extracted with 5% formic acid/50% acetonitrile (v/v) and concentrated to a small droplet using vacuum centrifugation. Desalting of peptides was done using hand-packed SPE Empore C18 Extraction Disks (aka Stage Tips, 3 M. St. Paul, MN, USA) as described (*97*). Desalted peptides were again concentrated and reconstituted in 10 μl 0.1% formic acid in water. An aliquot of the peptides was analyzed by nano–liquid chromatography-tandem MS (LC-MS/MS) using an Easy nLC 1,000 equipped with a self-packed 75 μm by 20 cm reverse-phase column (ReproSil-Pur C18, 3 m, Dr. Maisch GmbH, Germany) coupled online to a QExactive HF Orbitrap mass spectrometer via a Nanospray Flex source (all instruments from Thermo Fisher Scientific, Waltham, MA, USA). Analytical column temperature was maintained at 50°C by a column oven (Sonation GmBH, Germany). Peptides were eluted with a 3 to 40% acetonitrile gradient over 60 min at a flow rate of 250 nl/min. The mass spectrometer was operated in the DDA mode with survey scans acquired at a resolution of 120,000 (at mass/charge ratio (m/z) 200) over a scan range of 300 to 1750 m/z. Up to 15 of the most fragmentation by higher-energy collisional dissociation with a normalized collision energy of 27. The maximum injection times for the survey and MS/MS scans were 60 ms. In addition, the ion target value for both scan modes was set to 3e6. All acquired mass spectra were first converted to mascot generic format files (mgf) using Proteome Discoverer 1.4 and generated mgf files searched against a human protein database (SwissProt, 20, 210 sequences, 2014) using Mascot (Matrix Science, London, UK; version 2.7.0 www.matrixscience.com). Decoy proteins are added to the search to allow for the calculation of false discovery rates. The search parameters are as follows: (i) two missed cleavage tryptic sites are allowed; (ii) precursor ion mass tolerance = 10 ppm; (iii) fragment ion mass tolerance = 0.3 Da; and (iv) variable protein modifications are allowed for methionine oxidation, deamidation of asparagine and glutamines, cysteine acrylamide derivatization and protein N-terminal acetylation. MudPit scoring is typically applied using significance threshold score $P < 0.01$. Decoy database search is always activated and, in general, for merged LC-MS/MS analysis of a gel lane with $P < 0.01$, false discovery rate for protein ID averaged around 1%.

Protein preparation for glide molecular docking

The cryo-EM structure of the v-ATPase was retrieved from the PDB (code: 6VQ7), and it was refined with Protein Preparation Wizard implemented in Maestro 12. The protein structure was imported into workspace and preprocessed to assign bond orders, add hydrogen atoms, create zero-order bonds to metals, create disulfide bonds, and delete water molecules beyond 5 Å from hetero groups. In addition, missing atoms in residues and missing loops were added using Prime to generate a complete protein structure [note: the 34 missing amino acids (R133 to G169) in the V0a1 subunit could not be built using Prime because of the size of the missing loop]. The protein structure was further refined via automated H-bond assignment and restrained minimization with OPLS 2005 force field by converging heavy atoms to 0.3 Å RMSD. The N-terminal domain of the V0a1 subunit (E2 to Y363) was retrieved by deleting other subunits. The missing loop (R133 to G169) was built using the 3D builder module in Maestro 12, and the complete N-terminal domain of the V0a1 subunit was further refined with Protein Preparation Wizard. The folding states of the missing loop were searched by MD simulation using the Amber Molecular Dynamics Package. The truncated protein structure (N111 to V271) with ACE and NME terminal caps was solvated with the Amber ff14SB force field and TIP3P explicit water model in an octahedron periodic box using a buffer distance of 14.0 Å containing 150 mM NaCl in 20,827 water molecules. The solvated protein structure was treated to three consecutive minimization stages: (i) 1000 steps of steepest descent and 1000 steps of conjugate gradient minimization with 100 kcal mol^{-1} $Å^{-2}$ restraints on all atoms except water molecules; (ii) 2500 steps of steepest descent and 2500 steps of conjugate gradient minimization without restraints; and (iii) 1000 steps of steepest descent and 2500 steps of conjugate minimization with 100 kcal mol^{-1} $Å^{-2}$ restraints on N111 to F130 and Q252 to V271, which are helix units connected to the rest of the V0a1 subunit. After minimization, equilibration of the solvated protein was performed at 303.15 K for 100 ns under constant volume, with a timestep of 2 fs, and with SHAKE algorithm used to restrain on calculation of forces of bonds containing hydrogen atoms. In the equilibration, amide backbones of N112 to K129 and F170 to V271 were fixed with 10 kcal mol^{-1} $Å^{-2}$ restraints. The last frame of the MD equilibration was extracted from the simulation trajectories using the CPPTRAJ program in the AmberTools20, and it was subjected to the Glide docking after removing water molecules and ions.

Glide molecular docking and MD simulations

The last frame of the MD simulation was refined by Protein Preparation Wizard, and a protein grid for Glide dock was generated. Van der Waals radius was scaled by decreasing the default value of scaling factor to 0.8 to soften the potential for nonpolar parts of the receptor. The length of the inner box was increased to 20 $Å^3$ from the default value (10 $Å^3$) to explore all available binding sites of the target protein in the molecular docking. A ligand structure (NGpYEN) was built using the three-dimensional build module and the N- and C-terminal amino acids were capped with the acetyl group (ACE) and N-methylamine (NMA) in the refinement step, respectively. Glide software (v 8.7) in Maestro 12 was used to dock the ligand structure to the protein grid in the standard precision mode with the OPLS 2005 force field. The ligand structure was flexibly docked by sampling rotatable bonds, nitrogen inversions, and ring conformations. For the output of Glide docking, 200 poses were included for post-docking minimization, and 95 binding poses of the NGpYEN structure were obtained. After visual analysis by considering docking scores, 16 diverse binding poses of the NGpYEN structure at multiple binding sites were selected for further modeling with MD. Each complex structure of the truncated V0a1 with each binding pose of NGpYEN was solvated with TIP3P explicit water model in an octahedron periodic box using a buffer distance of 14.0 Å containing 150 mM NaCl in ca. 13,000 water molecules. Amber ff14SB and phosaa14SB force fields were applied to the solvated protein-ligand complex for MD simulation. Minimization and equilibration of the solvated protein-ligand complexes were conducted for 10 ns with the same parameters and constraints aforementioned. The last frame of the equilibration was obtained from the trajectories, and additional amino acids were added to the ligand structure in Maestro 12. Multiple minimization and equilibration were iteratively conducted for 480 ns with the same parameters and various constraints. VMD software was used to visually analyze the trajectories, and the binding pose of the ligand that showed similar binding pattern to the known structure of pY to its pocket (fig. S7A) was selected. Figures were generated using Pymol (The PyMOL Molecular Graphics System, Version 2.0 Schrodinger, LLC).

Estimation of binding affinity using MM-GBSA

The binding free energies of the V0a1 model structure in complex with phosphorylated and unphosphorylated ligands were estimated by Molecular mechnics with generalized Born surface area continuum solvation method (MM-GBSA). The truncated V0a1, a phosphorylated ligand (ACE-MQQNGpYENPTYK-NMA) structure, was obtained from the previous restricted MD simulation followed by protein preparation in Maestro 12. The model structure without the phosphorylated Y was obtained by mutating pY to Y in Maestro 12. These model structures were solvated as described above, and the whole systems were minimized by 2500 steps of steepest descent and 2500 steps of conjugate gradient minimization without restraints. After minimization, the systems were heated from 0 to 303.15 K for 300 ps and equilibrated for 100 ps under NVT condition followed by another equilibration for 100 ps under NPT condition. Last, 10 ns production run for each system was executed at a constant pressure (1 bar) and a constant temperature (303.15 K). The estimated binding free energy of each system was calculated with all trajectories (1000 frames) of the complexes.

Quantification and statistical analysis

All quantitative data were subjected to two-tailed unpaired Student's *t* test for single comparison, or one-way analysis of variance (ANOVA) analysis for multiple comparisons with Šidák's analysis using GraphPad Prism 9. For cellular data, three or more biological replicates with mean ± SEM were represented in bar graph with individual dots. Differences were considered significant with $P < 0.05$. Statistical parameters, including the definitions and value of sample size (n), deviations and P values, are reported in the corresponding figure legends. Statistically significance is represented with asterisks or hatch marks * or $^{\#}$, $P \leq 0.05$; ** or $^{\#\#}$, $P \leq 0.005$; *** or $^{\#\#\#}$, $P \leq 0.0005$; **** or $^{\#\#\#\#}$, $P \leq 0.0001$.

Supplementary Materials

This PDF file includes:

Figs. S1 to S10
Tables S1 to S3
Legend for data S1
References

Other Supplementary Material for this manuscript includes the following:

Data S1

REFERENCES AND NOTES

1. D. S. Knopman, H. Amieva, R. C. Petersen, G. Chételat, D. M. Holtzman, B. T. Hyman, R. A. Nixon, D. T. Jones, Alzheimer disease. *Nat. Rev. Dis. Primers* **7**, 33 (2021).
2. R. A. Nixon, The role of autophagy in neurodegenerative disease. *Nat. Med.* **19**, 983–997 (2013).
3. I. Lauritzen, R. Pardossi-Piquard, A. Bourgeois, S. Pagnotta, M. G. Biferi, M. Barkats, P. Lacor, W. Klein, C. Bauer, F. Checler, Intraneuronal aggregation of the β-CTF fragment of APP (C99) induces Aβ-independent lysosomal-autophagic pathology. *Acta Neuropathol.* **132**, 257–276 (2016).
4. R. Tamayev, S. Matsuda, O. Arancio, L. D'Adamio, β- but not γ-secretase proteolysis of APP causes synaptic and memory deficits in a mouse model of dementia. *EMBO Mol. Med.* **4**, 171–179 (2012).
5. Y. Jiang, Y. Sato, E. Im, M. Berg, M. Bordi, S. Darji, A. Kumar, P. S. Mohan, U. Bandyopadhyay, A. Diaz, A. M. Cuervo, R. A. Nixon, Lysosomal Dysfunction in Down Syndrome Is APP-Dependent and Mediated by APP-βCTF (C99). *J. Neurosci.* **39**, 5255–5268 (2019).
6. R. A. Nixon, D. S. Yang, J. H. Lee, Neurodegenerative lysosomal disorders: A continuum from development to late age. *Autophagy* **4**, 590–599 (2008).
7. A. M. Cataldo, C. M. Peterhoff, S. D. Schmidt, N. B. Terio, K. Duff, M. Beard, P. M. Mathews, R. A. Nixon, Presenilin mutations in familial Alzheimer disease and transgenic mouse models accelerate neuronal lysosomal pathology. *J. Neuropathol. Exp. Neurol.* **63**, 821–830 (2004).
8. F. Checler, E. Afram, R. Pardossi-Piquard, I. Lauritzen, Is γ-secretase a beneficial inactivating enzyme of the toxic APP C-terminal fragment C99? *J. Biol. Chem.* **296**, 100489 (2021).
9. R. A. Nixon, Autophagy, amyloidogenesis and Alzheimer disease. *J. Cell Sci.* **120**, 4081–4091 (2007).
10. Y. Wang, M. Martinez-Vicente, U. Krüger, S. Kaushik, E. Wong, E. M. Mandelkow, A. M. Cuervo, E. Mandelkow, Tau fragmentation, aggregation and clearance: the dual role of lysosomal processing. *Hum. Mol. Genet.* **18**, 4153–4170 (2009).
11. B. Boland, W. H. Yu, O. Corti, B. Mollereau, A. Henriques, E. Bezard, G. M. Pastores, D. C. Rubinsztein, R. A. Nixon, M. R. Duchen, G. R. Mallucci, G. Kroemer, B. Levine, E. L. Eskelinen, F. Mochel, M. Spedding, C. Louis, O. R. Martin, M. J. Millan, Promoting the clearance of neurotoxic proteins in neurodegenerative disorders of ageing. *Nat. Rev. Drug Discov.* **17**, 660–688 (2018).
12. J. Hwang, C. M. Estick, U. S. Ikonne, D. Butler, M. C. Pait, L. H. Elliott, S. Ruiz, K. Smith, K. M. Rentschler, C. Mundell, M. F. Almeida, N. S. Bear, J. P. Locklear, Y. Abumohsen, C. M. Ivey, K. L. G. Farizatto, B. A. Bahr, The Role of Lysosomes in a Broad Disease-Modifying Approach Evaluated across Transgenic Mouse Models of Alzheimer's Disease and Parkinson's Disease and Models of Mild Cognitive Impairment. *Int. J. Mol. Sci.* **20**, 4432 (2019).
13. J. H. Lee, M. V. Rao, D. S. Yang, P. Stavrides, E. Im, A. Pensalfini, C. Huo, P. Sarkar, T. Yoshimori, R. A. Nixon, Transgenic expression of a ratiometric autophagy probe specifically in neurons enables the interrogation of brain autophagy in vivo. *Autophagy* **15**, 543–557 (2019).
14. J. A. Mindell, Lysosomal acidification mechanisms. *Annu. Rev. Physiol.* **74**, 69–86 (2012).
15. A. Ballabio, J. S. Bonifacino, Lysosomes as dynamic regulators of cell and organismal homeostasis. *Nat. Rev. Mol. Cell Biol.* **21**, 101–118 (2020).
16. P. P. Y. Lie, L. Yoo, C. N. Goulbourne, M. J. Berg, P. Stavrides, C. Huo, J.-H. Lee, R. A. Nixon, Axonal transport of late endosomes and amphisomes is selectively modulated by local Ca^{2+} efflux and disrupted by PSEN1 loss of function. *Sci. Adv.* **8**, eabj5716 (2022).
17. M. Forgac, Vacuolar ATPases: Rotary proton pumps in physiology and pathophysiology. *Nat. Rev. Mol. Cell Biol.* **8**, 917–929 (2007).
18. K. Cotter, L. Stransky, C. McGuire, M. Forgac, Recent insights into the structure, regulation, and function of the V-ATPases. *Trends Biochem. Sci.* **40**, 611–622 (2015).
19. R. Liberman, S. Bond, M. G. Shainheit, M. J. Stadecker, M. Forgac, Regulated assembly of vacuolar ATPase is increased during cluster disruption-induced maturation of dendritic cells through a phosphatidylinositol 3-kinase/mTOR-dependent pathway. *J. Biol. Chem.* **289**, 1355–1363 (2014).
20. L. A. Stransky, M. Forgac, Amino Acid Availability Modulates Vacuolar H+-ATPase Assembly. *J. Biol. Chem.* **290**, 27360–27369 (2015).
21. J. Zhao, S. Benlekbir, J. L. Rubinstein, Electron cryomicroscopy observation of rotational states in a eukaryotic V-ATPase. *Nature* **521**, 241–245 (2015).
22. R. Zoncu, L. Bar-Peled, A. Efeyan, S. Wang, Y. Sancak, D. M. Sabatini, mTORC1 senses lysosomal amino acids through an inside-out mechanism that requires the vacuolar H(+)-ATPase. *Science* **334**, 678–683 (2011).
23. G. E. Mortimore, C. M. Schworer, Induction of autophagy by amino-acid deprivation in perfused rat liver. *Nature* **270**, 174–176 (1977).
24. D. J. Colacurcio, R. A. Nixon, Disorders of lysosomal acidification-The emerging role of v-ATPase in aging and neurodegenerative disease. *Ageing Res. Rev.* **32**, 75–88 (2016).
25. J. H. Lee, W. H. Yu, A. Kumar, S. Lee, P. S. Mohan, C. M. Peterhoff, D. M. Wolfe, M. Martinez-Vicente, A. C. Massey, G. Sovak, Y. Uchiyama, D. Westaway, A. M. Cuervo, R. A. Nixon, Lysosomal proteolysis and autophagy require presenilin 1 and are disrupted by Alzheimer-related PS1 mutations. *Cell* **141**, 1146–1158 (2010).
26. J.-H. Lee, D.-S. Yang, C. N. Goulbourne, E. Im, P. Stavrides, A. Pensalfini, H. Chan, C. Bouchet-Marquis, C. Bleiwas, M. J. Berg, C. Huo, J. Peddy, M. Pawlik, E. Levy, M. Rao, M. Staufenbiel, R. A. Nixon, Faulty autolysosome acidification in Alzheimer's disease mouse models induces autophagic build-up of Aβ in neurons, yielding senile plaques. *Nat. Neurosci.* **25**, 688–701 (2022).
27. Z. Diwu, C. S. Chen, C. Zhang, D. H. Klaubert, R. P. Haugland, A novel acidotropic pH indicator and its potential application in labeling acidic organelles of live cells. *Chem. Biol.* **6**, 411–418 (1999).
28. M. W. Walker, E. Lloyd-Evans, A rapid method for the preparation of ultrapure, functional lysosomes using functionalized superparamagnetic iron oxide nanoparticles. *Methods Cell Biol.* **126**, 21–43 (2015).
29. S. Kim, Y. Sato, P. S. Mohan, C. Peterhoff, A. Pensalfini, A. Rigoglioso, Y. Jiang, R. A. Nixon, Evidence that the rab5 effector APPL1 mediates APP-βCTF-induced dysfunction of endosomes in Down syndrome and Alzheimer's disease. *Mol. Psychiatry* **21**, 707–716 (2016).
30. M. Pera, D. Alcolea, R. Sánchez-Valle, C. Guardia-Laguarta, M. Colom-Cadena, N. Badiola, M. Suárez-Calvet, A. Lladó, A. A. Barrera-Ocampo, D. Sepulveda-Falla, R. Blesa, J. L. Molinuevo, J. Clarimón, I. Ferrer, E. Gelpi, A. Lleó, Distinct patterns of APP processing in the CNS in autosomal-dominant and sporadic Alzheimer disease. *Acta Neuropathol.* **125**, 201–213 (2013).
31. Y. Jiang, K. A. Mullaney, C. M. Peterhoff, S. Che, S. D. Schmidt, A. Boyer-Boiteau, S. D. Ginsberg, A. M. Cataldo, P. M. Mathews, R. A. Nixon, Alzheimer's-related endosome dysfunction in Down syndrome is Abeta-independent but requires APP and is reversed by BACE-1 inhibition. *Proc. Natl. Acad. Sci. U.S.A.* **107**, 1630–1635 (2010).
32. S. E. Hoey, R. J. Williams, M. S. Perkinton, Synaptic NMDA receptor activation stimulates alpha-secretase amyloid precursor protein processing and inhibits amyloid-beta production. *J. Neurosci.* **29**, 4442–4460 (2009).
33. D. Del Prete, F. Lombino, X. Liu, L. D'Adamio, APP is cleaved by Bace1 in pre-synaptic vesicles and establishes a pre-synaptic interactome, via its intracellular domain, with molecular complexes that regulate pre-synaptic vesicles functions. *PLOS ONE* **9**, e108576 (2014).
34. O. Söderberg, M. Gullberg, M. Jarvius, K. Ridderstråle, K.-J. Leuchowius, J. Jarvius, K. Wester, P. Hydbring, F. Bahram, L.-G. Larsson, U. Landegren, Direct observation of individual endogenous protein complexes in situ by proximity ligation. *Nat. Methods* **3**, 995–1000 (2006).
35. K. Ando, K. I. Iijima, J. I. Elliott, Y. Kirino, T. Suzuki, Phosphorylation-dependent regulation of the interaction of amyloid precursor protein with Fe65 affects the production of beta-amyloid. *J. Biol. Chem.* **276**, 40353–40361 (2001).
36. S. Das, M. Raychaudhuri, U. Sen, D. Mukhopadhyay, Functional implications of the conformational switch in AICD peptide upon binding to Grb2-SH2 domain. *J. Mol. Biol.* **414**, 217–230 (2011).
37. J. Radzimanowski, B. Simon, M. Sattler, K. Beyreuther, I. Sinning, K. Wild, Structure of the intracellular domain of the amyloid precursor protein in complex with Fe65-PTB2. *EMBO Rep.* **9**, 1134–1140 (2008).
38. C. Russo, S. Salis, V. Dolcini, V. Venezia, X. Song, J. K. Teller, G. Schettini, Amino-terminal modification and tyrosine phosphorylation of [corrected] carboxy-terminal fragments of the amyloid precursor protein in Alzheimer's disease and Down's syndrome brain. *Neurobiol. Dis.* **8**, 173–180 (2001).
39. F. Iannuzzi, R. Sirabella, N. Canu, T. J. Maier, L. Annunziato, C. Matrone, Fyn Tyrosine Kinase Elicits Amyloid Precursor Protein Tyr682 Phosphorylation in Neurons from Alzheimer's Disease Patients. *Cell* **9**, 1807 (2020).
40. Y. M. Abbas, D. Wu, S. A. Bueler, C. V. Robinson, J. L. Rubinstein, Structure of V-ATPase from the mammalian brain. *Science* **367**, 1240–1246 (2020).

41. D. A. Case, T. E. Cheatham 3rd, T. Darden, H. Gohlke, R. Luo, K. M. Merz Jr., A. Onufriev, C. Simmerling, B. Wang, R. J. Woods, The Amber biomolecular simulation programs. *J. Comput. Chem.* **26**, 1668–1688 (2005).
42. T. A. Halgren, R. B. Murphy, R. A. Friesner, H. S. Beard, L. L. Frye, W. T. Pollard, J. L. Banks, Glide: A new approach for rapid, accurate docking and scoring. 2. Enrichment factors in database screening. *J. Med. Chem.* **47**, 1750–1759 (2004).
43. V. Tsui, D. A. Case, Theory and applications of the generalized Born solvation model in macromolecular simulations. *Biopolymers* **56**, 275–291 (2000).
44. E. T. Poulsen, F. Iannuzzi, H. F. Rasmussen, T. J. Maier, J. J. Enghild, A. L. Jørgensen, C. Matrone, RETRACTED An Aberrant Phosphorylation of Amyloid Precursor Protein Tyrosine Regulates Its Trafficking and the Binding to the Clathrin Endocytic Complex in Neural Stem Cells of Alzheimer's Disease Patients. *Front. Mol. Neurosci.* **10**, 59 (2017).
45. A. J. Villar, P. V. Belichenko, A. M. Gillespie, H. M. Kozy, W. C. Mobley, C. J. Epstein, Identification and characterization of a new Down syndrome model, Ts[Rb(12.1716)]2Cje, resulting from a spontaneous Robertsonian fusion between T(171)65Dn and mouse chromosome 12. *Mamm. Genome* **16**, 79–90 (2005).
46. A. M. Cataldo, S. Petanceska, C. M. Peterhoff, N. B. Terio, C. J. Epstein, A. Villar, E. J. Carlson, M. Staufenbiel, R. A. Nixon, App gene dosage modulates endosomal abnormalities of Alzheimer's disease in a segmental trisomy 16 mouse model of down syndrome. *J. Neurosci.* **23**, 6788–6792 (2003).
47. A. M. Cataldo, J. L. Barnett, C. Pieroni, R. A. Nixon, Increased neuronal endocytosis and protease delivery to early endosomes in sporadic Alzheimer's disease: Neuropathologic evidence for a mechanism of increased beta-amyloidogenesis. *J. Neurosci.* **17**, 6142–6151 (1997).
48. Y. Jiang, A. Rigoglioso, C. M. Peterhoff, M. Pawlik, Y. Sato, C. Bleiwas, P. Stavrides, J. F. Smiley, S. D. Ginsberg, P. M. Mathews, E. Levy, R. A. Nixon, Partial BACE1 reduction in a Down syndrome mouse model blocks Alzheimer-related endosomal anomalies and cholinergic neurodegeneration: Role of APP-CTF. *Neurobiol. Aging* **39**, 90–98 (2016).
49. A. C. Kaufman, S. V. Salazar, L. T. Haas, J. Yang, M. A. Kostylev, A. T. Jeng, S. A. Robinson, E. C. Gunther, C. H. van Dyck, H. B. Nygaard, S. M. Strittmatter, Fyn inhibition rescues established memory and synapse loss in Alzheimer mice. *Ann. Neurol.* **77**, 953–971 (2015).
50. C. Hirata-Fukae, H.-F. Li, H.-S. Hoe, A. J. Gray, S. S. Minami, K. Hamada, T. Niikura, F. Hua, H. Tsukagoshi-Nagai, Y. Horikoshi-Sakuraba, M. Mughal, G. W. Rebeck, F. M. LaFerla, M. P. Mattson, N. Iwata, T. C. Saido, W. L. Klein, K. E. Duff, P. S. Aisen, Y. Matsuoka, Females exhibit more extensive amyloid, but not tau, pathology in an Alzheimer transgenic model. *Brain Res.* **1216**, 92–103 (2008).
51. L. M. Tai, J. Maldonado Weng, M. J. LaDu, S. T. Brady, Relevance of transgenic mouse models for Alzheimer's disease. *Prog. Mol. Biol. Transl. Sci.* **177**, 1–48 (2021).
52. M. H. Česen, K. Pegan, A. Spes, B. Turk, Lysosomal pathways to cell death and their therapeutic applications. *Exp. Cell Res.* **318**, 1245–1251 (2012).
53. M. F. Almeida, B. A. Bahr, S. T. Kinsey, Endosomal-lysosomal dysfunction in metabolic diseases and Alzheimer's disease. *Int. Rev. Neurobiol.* **154**, 303–324 (2020).
54. R. A. Nixon, D. S. Yang, Autophagy and neuronal cell death in neurological disorders. *Cold Spring Harb. Perspect. Biol.* **4**, a008839 (2012).
55. E. Doran, D. Keator, E. Head, M. J. Phelan, R. Kim, M. Totoiu, J. R. Barrio, G. W. Small, S. G. Potkin, I. T. Lott, Down Syndrome, Partial Trisomy 21, and Absence of Alzheimer's Disease: The Role of APP. *J. Alzheimers Dis.* **56**, 459–470 (2017).
56. D. J. Colacurcio, A. Pensalfini, Y. Jiang, R. A. Nixon, Dysfunction of autophagy and endosomal-lysosomal pathways: Roles in pathogenesis of Down syndrome and Alzheimer's Disease. *Free Radic. Biol. Med.* **114**, 40–51 (2018).
57. I. T. Lott, E. Head, Dementia in Down syndrome: Unique insights for Alzheimer disease research. *Nat. Rev. Neurol.* **15**, 135–147 (2019).
58. B. De Strooper, Loss-of-function presenilin mutations in Alzheimer disease. Talking Point on the role of presenilin mutations in Alzheimer disease. *EMBO Rep.* **8**, 141–146 (2007).
59. J.-H. Lee, M. K. McBrayer, D. M. Wolfe, L. J. Haslett, A. Kumar, Y. Sato, P. P. Y. Lie, P. Mohan, E. E. Coffey, U. Kompella, C. H. Mitchell, E. Lloyd-Evans, R. A. Nixon, Presenilin 1 maintains lysosomal Ca(2+) homeostasis via TRPML1 by regulating vATPase-mediated lysosome acidification. *Cell Rep.* **12**, 1430–1444 (2015).
60. R. Wallings, N. Connor-Robson, R. Wade-Martins, LRRK2 interacts with the vacuolar-type H+-ATPase pump a1 subunit to regulate lysosomal function. *Hum. Mol. Genet.* **28**, 2696–2710 (2019).
61. M. B. Bagh, S. Peng, G. Chandra, Z. Zhang, S. P. Singh, N. Pattabiraman, A. Liu, A. B. Mukherjee, Misrouting of v-ATPase subunit V0a1 dysregulates lysosomal acidification in a neurodegenerative lysosomal storage disease model. *Nat. Commun.* **8**, 14612 (2017).
62. A. M. Cataldo, P. M. Mathews, A. B. Boiteau, L. C. Hassinger, C. M. Peterhoff, Y. Jiang, K. Mullaney, R. L. Neve, J. Gruenberg, R. A. Nixon, Down syndrome fibroblast model of Alzheimer-related endosome pathology: Accelerated endocytosis promotes late endocytic defects. *Am. J. Pathol.* **173**, 370–384 (2008).
63. N. Zambrano, P. Bruni, G. Minopoli, R. Mosca, D. Molino, C. Russo, G. Schettini, M. Sudol, T. Russo, The beta-amyloid precursor protein APP is tyrosine-phosphorylated in cells expressing a constitutively active form of the Abl protoncogene. *J. Biol. Chem.* **276**, 19787–19792 (2001).
64. P. E. Tarr, C. Contursi, R. Roncarati, C. Noviello, E. Ghersi, M. H. Scheinfeld, N. Zambrano, T. Russo, L. D'Adamio, Evidence for a role of the nerve growth factor receptor TrkA in tyrosine phosphorylation and processing of beta-APP. *Biochem. Biophys. Res. Commun.* **295**, 324–329 (2002).
65. H.-S. Hoe, S. S. Minami, A. Makarova, J. Lee, B. T. Hyman, Y. Matsuoka, G. W. Rebeck, Fyn modulation of Dab1 effects on amyloid precursor protein and ApoE receptor 2 processing. *J. Biol. Chem.* **283**, 6288–6299 (2008).
66. G. J. Ho, M. Hashimoto, A. Adame, M. Izu, M. F. Alford, L. J. Thal, L. A. Hansen, E. Masliah, Altered p59Fyn kinase expression accompanies disease progression in Alzheimer's disease: Implications for its functional role. *Neurobiol. Aging* **26**, 625–635 (2005).
67. C. De Jonghe, C. Esselens, S. Kumar-Singh, K. Craessaerts, S. Serneels, F. Checler, W. Annaert, C. Van Broeckhoven, B. De Strooper, Pathogenic APP mutations near the gamma-secretase cleavage site differentially affect Abeta secretion and APP C-terminal fragment stability. *Hum. Mol. Genet.* **10**, 1665–1671 (2001).
68. A. Salehi, J. D. Delcroix, P. V. Belichenko, K. Zhan, C. Wu, J. S. Valletta, R. Takimoto-Kimura, A. M. Kleschevnikov, K. Sambamurti, P. P. Chung, W. Xia, A. Villar, W. A. Campbell, L. S. Kulnane, R. A. Nixon, B. T. Lamb, C. J. Epstein, G. B. Stokin, L. S. B. Goldstein, W. C. Mobley, Increased App expression in a mouse model of Down's syndrome disrupts NGF transport and causes cholinergic neuron degeneration. *Neuron* **51**, 29–42 (2006).
69. G. Woodruff, S. M. Reyna, M. Dunlap, R. van der Kant, J. A. Callender, J. E. Young, E. A. Roberts, L. S. B. Goldstein, Defective Transcytosis of APP and Lipoproteins in Human iPSC-Derived Neurons with Familial Alzheimer's Disease Mutations. *Cell Rep.* **17**, 759–773 (2016).
70. L.-B. Yang, K. Lindholm, R. Yan, M. Citron, W. Xia, X.-L. Yang, T. Beach, L. Sue, P. Wong, D. Price, R. Li, Y. Shen, Elevated beta-secretase expression and enzymatic activity detected in sporadic Alzheimer disease. *Nat. Med.* **9**, 3–4 (2003).
71. G. Zuliani, A. Trentini, V. Rosta, R. Guerrini, S. Pacifico, S. Bonazzi, A. Guiotto, A. Passaro, D. Seripa, G. Valacchi, C. Cervellati, Increased blood BACE1 activity as a potential common pathogenic factor of vascular dementia and late onset Alzheimer's disease. *Sci. Rep.* **10**, 14980 (2020).
72. M. J. Yáñez, O. Belbin, L. D. Estrada, N. Leal, P. S. Contreras, A. Lleó, P. V. Burgos, S. Zanlungo, A. R. Alvarez, c-Abl links APP-BACE1 interaction promoting APP amyloidogenic processing in Niemann-Pick type C disease. *Biochim. Biophys. Acta* **1862**, 2158–2167 (2016).
73. R. Shen, X. Zhao, L. He, Y. Ding, W. Xu, S. Lin, S. Fang, W. Yang, K. Sung, B. Spencer, R. A. Rissman, M. Lei, J. Ding, C. Wu, Upregulation of RIN3 induces endosomal dysfunction in Alzheimer's disease. *Transl. Neurodegener.* **9**, 26 (2020).
74. Z. Wang, Q. Zhang, J.-R. Lin, M. R. Jabalameli, J. Mitra, N. Nguyen, Z. D. Zhang, Deep post-GWAS analysis identifies potential risk genes and risk variants for Alzheimer's disease, providing new insights into its disease mechanisms. *Sci. Rep.* **11**, 20511 (2021).
75. D. A. Butterfield, F. Di Domenico, A. M. Swomley, E. Head, M. Perluigi, Redox proteomics analysis to decipher the neurobiology of Alzheimer-like neurodegeneration: Overlaps in Down's syndrome and Alzheimer's disease brain. *Biochem. J.* **463**, 177–189 (2014).
76. M. Perluigi, D. A. Butterfield, Oxidative Stress and Down Syndrome: A Route toward Alzheimer-Like Dementia. *Curr. Gerontol. Geriatr. Res.* **2012**, 724904 (2012).
77. R. A. Nixon, The aging lysosome: An essential catalyst for late-onset neurodegenerative diseases. *Biochim. Biophys. Acta Proteins Proteom.* **1868**, 140443 (2020).
78. J. H. K. Tam, M. R. Cobb, C. Seah, S. H. Pasternak, Tyrosine binding protein sites regulate the intracellular trafficking and processing of amyloid precursor protein through a novel lysosome-directed pathway. *PLOS ONE* **11**, e0161445 (2016).
79. Y. Tian, J. C. Chang, P. Greengard, M. Flajolet, The convergence of endosomal and autophagosomal pathways: Implications for APP-CTF degradation. *Autophagy* **10**, 694–696 (2014).
80. G. R. Richo, G. E. Conner, Structural requirements of procathepsin D activation and maturation. *J. Biol. Chem.* **269**, 14806–14812 (1994).
81. R. Singh, S. Kaushik, Y. Wang, Y. Xiang, I. Novak, M. Komatsu, K. Tanaka, A. M. Cuervo, M. J. Czaja, Autophagy regulates lipid metabolism. *Nature* **458**, 1131–1135 (2009).
82. T. Asano, M. Komatsu, Y. Yamaguchi-Iwai, F. Ishikawa, N. Mizushima, K. Iwai, Distinct mechanisms of ferritin delivery to lysosomes in iron-depleted and iron-replete cells. *Mol. Cell. Biol.* **31**, 2040–2052 (2011).
83. N. Nakamura, A. Matsuura, Y. Wada, Y. Ohsumi, Acidification of vacuoles is required for autophagic degradation in the yeast, Saccharomyces cerevisiae. *J. Biochem.* **121**, 338–344 (1997).
84. I. Kukic, S. L. Kelleher, K. Kiselyov, Zn2+ efflux through lysosomal exocytosis prevents Zn2+–induced toxicity. *J. Cell Sci.* **127**, 3094–3103 (2014).

85. P. P. Y. Lie, D.-S. Yang, P. Stavrides, C. N. Goulbourne, P. Zheng, P. S. Mohan, A. M. Cataldo, R. A. Nixon, Post-Golgi carriers, not lysosomes, confer lysosomal properties to pre-degradative organelles in normal and dystrophic axons. *Cell Rep.* **35**, 109034 (2021).
86. C. McGuire, L. Stransky, K. Cotter, M. Forgac, Regulation of V-ATPase activity. *Front. Biosci. (Landmark Ed.)* **22**, 609–622 (2017).
87. L. Wang, D. Wu, C. V. Robinson, H. Wu, T. M. Fu, Structures of a Complete Human V-ATPase Reveal Mechanisms of Its Assembly. *Mol. Cell* **80**, 501–511.e3 (2020).
88. Y.-S. Jung, S. Jun, M. J. Kim, S. H. Lee, H. N. Suh, E. M. Lien, H.-Y. Jung, S. Lee, J. Zhang, J.-I. Yang, H. Ji, J. Y. Wu, W. Wang, R. K. Miller, J. Chen, P. D. McCrea, S. Kopetz, J.-I. Park, TMEM9 promotes intestinal tumorigenesis through vacuolar-ATPase-activated Wnt/β-catenin signalling. *Nat. Cell Biol.* **20**, 1421–1433 (2018).
89. B. Zhong, M. Liu, C. Bai, Y. Ruan, Y. Wang, L. Qiu, Y. Hong, X. Wang, L. Li, B. Li, Caspase-8 Induces Lysosome-Associated Cell Death in Cancer Cells. *Mol. Ther.* **28**, 1078–1091 (2020).
90. Z. A. Klein, H. Takahashi, M. Ma, M. Stagi, M. Zhou, T. K. T. Lam, S. M. Strittmatter, Loss of TMEM106B Ameliorates Lysosomal and Frontotemporal Dementia-Related Phenotypes in Progranulin-Deficient Mice. *Neuron* **95**, 281–296.e6 (2017).
91. R. A. Nixon, D.-S. Yang, Autophagy failure in Alzheimer's disease--locating the primary defect. *Neurobiol. Dis.* **43**, 38–45 (2011).
92. A. M. Cataldo, D. J. Hamilton, J. L. Barnett, P. A. Paskevich, R. A. Nixon, Properties of the endosomal-lysosomal system in the human central nervous system: Disturbances mark most neurons in populations at risk to degenerate in Alzheimer's disease. *J. Neurosci.* **16**, 186–199 (1996).
93. R. A. Nixon, Amyloid precursor protein and endosomal-lysosomal dysfunction in Alzheimer's disease: Inseparable partners in a multifactorial disease. *FASEB J.* **31**, 2729–2743 (2017).
94. M. Brouillard, P. Barthélémy, B. Dehay, S. Crauste-Manciet, V. Desvergnes, Nucleolipid Acid-Based Nanocarriers Restore Neuronal Lysosomal Acidification Defects. *Front. Chem.* **9**, 736554 (2021).
95. J. H. Lee, D. M. Wolfe, S. Darji, M. K. McBrayer, D. J. Colacurcio, A. Kumar, P. Stavrides, P. S. Mohan, R. A. Nixon, β2-adrenergic agonists rescue lysosome acidification and function in PSEN1 deficiency by reversing defective ER-to-lysosome delivery of ClC-7. *J. Mol. Biol.* **432**, 2633–2650 (2020).
96. P. P. Y. Lie, R. A. Nixon, Lysosome trafficking and signaling in health and neurodegenerative diseases. *Neurobiol. Dis.* **122**, 94–105 (2019).
97. J. Rappsilber, M. Mann, Y. Ishihama, Protocol for micro-purification, enrichment, pre-fractionation and storage of peptides for proteomics using StageTips. *Nat. Protoc.* **2**, 1896–1906 (2007).
98. P. M. Mathews, Y. Jiang, S. D. Schmidt, O. M. Grbovic, M. Mercken, R. A. Nixon, Calpain activity regulates the cell surface distribution of amyloid precursor protein. inhibition of calpains enhances endosomal generation of beta-cleaved C-terminal APP fragments. *J. Biol. Chem.* **277**, 36415–36424 (2002).

Acknowledgments: We thank K. Kim (Yonsei University, Republic of Korea) for advice on structural analyses. We are very grateful to E. Levy (Nathan S. Kline Institute; NYU Grossman School of Medicine) for supervising animal breeding and thank M. Pawlik, C. Huo, and S. DeRosa (Nathan S. Kline Institute) for maintaining animals. Human tissues were obtained from the Brain Bank for Developmental Disabilities and Aging. **Funding:** This study was supported by National Institute on Aging grants P01AG017617 (R.A.N.), R01AG062376 (R.A.N.), National Center for Research Resources grant S10 RR027990 (T.A.N.), and Queens College Start-up fund 90922-09 07 (J.Y.C.). **Author contributions:** Conceptualization: E.I., R.A.N., and Y.J. Methodology: E.I., R.A.N., J.Y.C., H.E.-B., T.A.N., and J.W. Investigation: E.I., P.H.S., S.D., H.E.-B., T.A.N., and J.Y.C. Visualization: E.I. Supervision: R.A.N. Writing—original draft: E.I. and R.A.N. Writing—review and editing: E.I., R.A.N., Y.J., J.-H.L., P.H.S., and J.Y.C. **Competing interests:** The authors declare that they have no competing interests. **Data and materials availability:** All data needed to evaluate the conclusions in the paper are present in the paper and/or the Supplementary Materials.

Submitted 23 December 2022
Accepted 23 June 2023
Published 26 July 2023
10.1126/sciadv.adg1925